Wang *et al. Genome Medicine* (2026) 18:63
https://doi.org/10.1186/s13073-026-01634-w

Genome Medicine

METHODOLOGY Open Access

Alignment of spatial transcriptomics slices across diseases, platforms and conditions

Yu Wang[1,2], Zaiyi Liu[3,4], Qingchen Zang[5] and Xiaoke Ma[1,2,6*]

Abstract
Spatial transcriptomics (ST) facilitates the exploration of biological tissue structures and functions within spatial context. Slice alignment and integration are prevalent for analyzing ST data, and current algorithms either focus on adjacent slices or require prior information to guide alignment, limits their applications for downstream analysis. Here, we present AlignDG, an information theory-based graph model that jointly aligns and integrates ST slices across diverse diseases, platforms and conditions without prior information. Experimental results demonstrate that AlignDG outperforms existing baselines in terms of precision, robustness, and efficiency with approximate 50% of slices, providing an effective alternative for analyzing ST data (code: https://github.com/xkmaxidian/AlignDG).

Keywords Spatial transcriptomics, Slice alignment, Integrative analysis, Optimal transport, Network biology

Background

Measurement of messenger RNA (mRNA) expression within native tissue architecture enables comprehensive analysis of cellular organization, not only deciphering molecular signatures across heterogeneous cell populations but also elucidating how spatial microenvironments modulate cellular functionality and structural integrity [1, 2]. Spatial transcriptomics (ST) technologies simultaneously measure gene expression by preserving spatial coordinates of units at various resolutions, i.e., 10× Visium [3] with 55 μm, Slide-seq [4, 5] with 10 μm, and Stereo-seq [6] with 220 nm. Most studies focus on single-condition ST data analysis, facilitating the exploration of bio-markers, spatial domains, cell-cell communications, and progression of cancers [7–15].

The inherent complexity of biological tissues poses significant challenges for systematic investigation of systems under uniform experimental conditions, and integrative analysis of omics data provides more comprehensive characterizations of tissues. For instance, the limited genome coverage of ST data can be complemented with single-cell RNA-sequencing (scRNA-seq) data, which is pivotal for elucidating complex biological mechanisms [16, 17]. And, integrating multiple ST slices associated with tissue development or cancer progression enables effective tracking of spatiotemporal patterns and their molecular underpinnings, which are critical for the diagnosis and therapy of complex diseases [18]. Consequently, there is a pressing need to integrate multiple ST datasets generated by various conditions, platforms, and

*Correspondence:
Xiaoke Ma
xkma@xidian.edu.cn
[1]School of Computer Science and Technology, Xidian University, No.2 South Taibai Road, Xi'an 710071, Shaanxi, China
[2]Key Laboratory of Smart Human-Computer Interaction and Wearable Technology of Shaanxi Province, Xidian University, No.2 South Taibai Road, Xi'an 710071, Shaanxi, China
[3]Department of Radiology, Guangdong Provincial People's Hospital (Guangdong Academy of Medical Sciences), Southern Medical University, 106 Zhongshan Er Road, Guangzhou 510080, Guangzhou, China
[4]Guangdong Provincial Key Laboratory of Artificial Intelligence in Medical Image Analysis and Application, Guangdong Provincial People's Hospital, Guangdong Academy of Medical Sciences, 106 Zhongshan Er Road, Guangzhou 510080, Guangzhou, China
[5]School of Computer Science and Technology, Hainan University, No. 58 Renmin Avenue, Haikou 570228, Hainan, China
[6]Shenzhen Loop Area Institute, No. 6 Hongmian Road, Fubao District, Shenzhen 518017, Guangdong, China

stages, thereby facilitating holistic interrogation of tissue architecture at various resolutions [19, 20].

The alignment of ST slices, which involves constructing mappings among spots across different slices, is a fundamental task in the integrative analysis of ST datasets. Accurate alignment enables the identification of conserved and slice-specific spatial domains, thereby facilitating downstream analyses [21–23]. However, aligning ST slices remains challenging because heterogeneity and batch effects across various datasets, which often obscure true biological signals and hinder data integration. Current algorithms for the integrative analysis of ST slices can be broadly categorized into non-spatial- and spatial-aware approaches. Non-spatial-aware methods ignore spatial information of spots by directly extending algorithms originally developed for scRNA-seq data, such as Seurat [24], canonical correlation analysis (CCA) [25], Harmony [26], and scVI [27]. These algorithms concentrate on learning features to fully represent expression profile of datasets, resulting in the low accuracy because of the neglect of spatial information.

Although classical image registration methods provide an alternative approach for aligning ST slices [28–30], these methods are primarily developed for histological and medical images, including functional magnetic resonance imaging (fMRI) [31]. Recent evidence [32] suggests that image registration is not easily extensible to ST data because the absence of corresponding histological images. Furthermore, most image registration algorithms are supervised, imposing extra burdens for users since manually selected landmarks are required [33]. To address these limitations, spatial-aware algorithms for aligning ST slices consider both spatial proximity and transcriptional similarity of spots across ST slices with various strategies. For example, STalign [34] and Spateo [35] utilize partially matched sections of tissues to guide alignment of slices, whereas SANTO [36] and CAST [37] deliberately leverage global spatial information of slices. SPACEL [38] aligns slices by exploiting meta-structure of spatial domains, and PASTE [39] (its variants PASTE2 [33] and DeST-OT [40]) hypothesize that topological similarity of spot graphs is sufficient to model correspondence of spots across slices. STAligner [41] employs graph neural networks (GNN) to learn features of spots by taking mutual nearest neighbors (MNN) [42] across slices as prior information. SLAT [43] performs slice alignment by using the graph adversarial discriminator [44], and Moscot [45] utilizes the low-rank optimal transport strategy to accelerate alignment of large-scale ST slices.

Although great progress has been achieved, critical challenges in ST slice alignment remain unsolved. First, existing algorithms primarily focus on aligning adjacent ST slices, such as consecutive slices of tissues and identical slices generated by various platforms, where extensive overlapping of slices provides strong prior information for alignment of slices. However, adjacent slice scenarios are not always feasible because of financial and technical limitations. In other words, distant ST slices, such as non-consecutive slices of tissues and slices collected across different developmental stages or organs (Fig. 1A) are ubiquitous, yet few attempts address this scenario. Second, most current algorithms first learn features of spots and then perform alignment of slices, implicitly assuming independence between feature learning and alignment of slices. In contrast, previous studies [15, 46] demonstrate that joint learning of representations and downstream tasks significantly improves quality of features, thereby improving performance of algorithms for analyzing ST data. Third, existing algorithms can only handle balanced slices, i.e., sizes or spatial structures of slices are highly similar, failing to address alignment of unbalanced ST slices, which severely limits their applicability in real-world scenarios. Therefore, there is a critical need for alternatives capable of aligning distant and unbalanced ST slices under diverse conditions.

To address these aforementioned problems, we propose a novel algorithm for *Align*ing *D*istant slices with *G*raph model (called *AlignDG*), which is a network-based approach for aligning distant ST slices. As shown in Fig. 1B, AlignDG consists of three major components, i.e., attributed multi-layer network construction, feature learning with graph model, and alignment of ST slices. To avoid independence of feature learning and slice alignment, AlignDG proposes a joint learning framework to integrate these tasks, where features are learned using GNN under the guidance of spot correspondences across slices. To handle unbalanced slices, AlignDG leverages an information-theoretic matching strategy that maximizes mutual information between spot distributions across slices, enabling a more precise alignment of distant ST slices. Moreover, AlignDG employs self-supervised learning to fully exploit the topological structure of spot networks, thereby enhancing both quality and discriminative of spot features. Experimental results demonstrate that AlignDG not only outperforms state-of-the-art baselines for alignment of ST slices without prior information, but also saves approximate 50% of slices required by current algorithms. Overall, AlignDG offers an effective alternative for integrative analysis of ST data.

Methods

AlignDG performs alignment of slices without prior information by leveraging the topological structure of spot attributed multi-layer networks, which consists of three major components, i.e., attributed multi-layer network construction, feature learning with graph model, and alignment of slices, where the latter two components

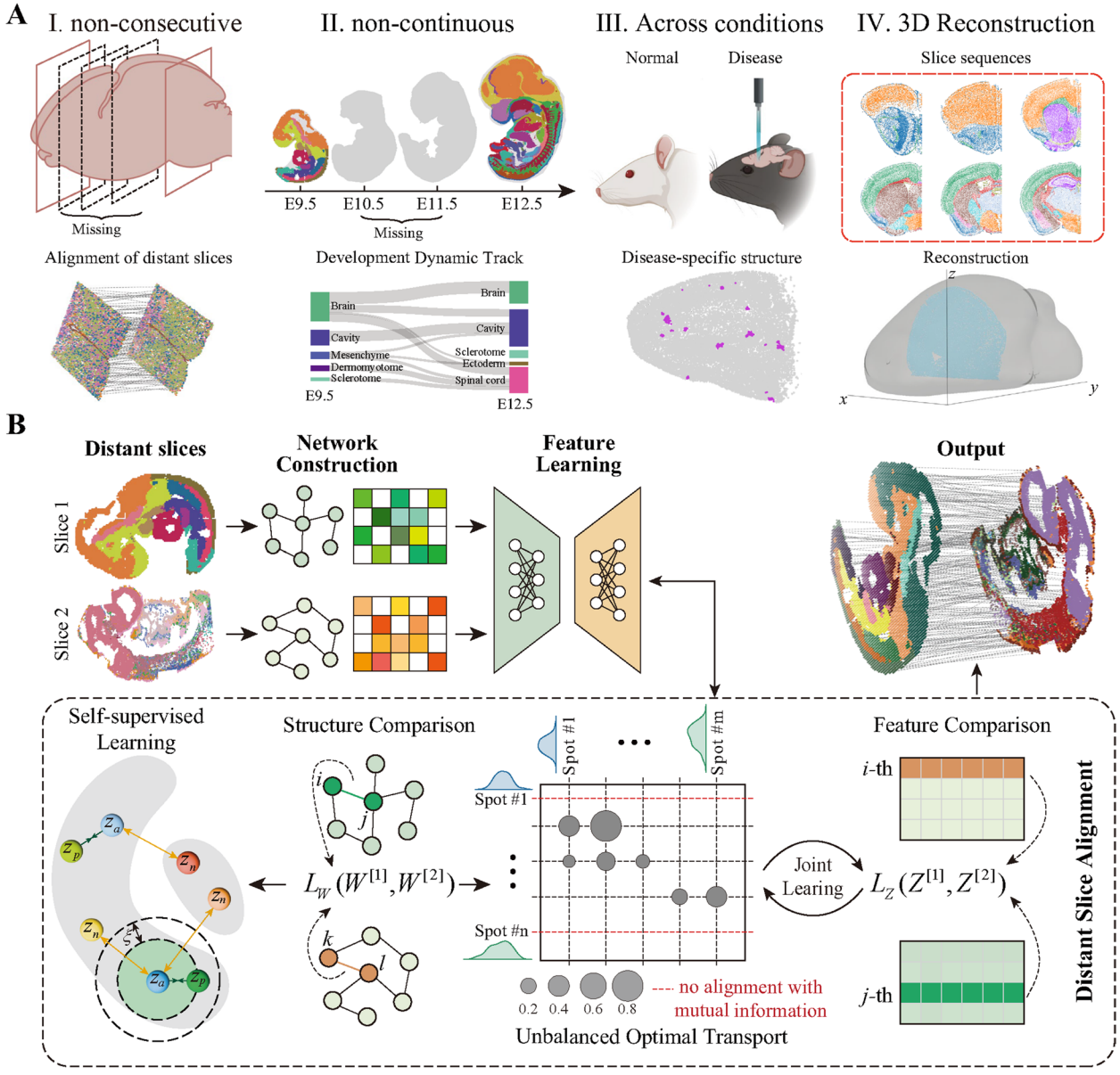

Fig. 1 Overview of AlignDG for distant slice alignment. **A** Typical circumstances of distant slices addressed by AlignDG, including non-consecutive slices of a tissue (I), slices associated with non-continuous developmental (embryonic) stages (II), slices with different conditions (III), and 3D reconstruction of tissues (IV), respectively. **B** AlignDG consists of network construction, feature learning, and distant slice alignment, where network construction takes the normalized gene expression and spatial coordinates of spots as input to obtain attributed multi-layer networks, and feature learning employs graph attention auto-encoder neural network to extract spatial-aware representation of spots. And, distant slice alignment simultaneously exploits feature and structure of attributed multi-layer networks to perform alignment across unbalanced and distant slices by measuring similarity of spots in terms of distributions of spots with mutual information, where self-supervised learning is utilized to improve discriminative of features with self-supervised prior information

are jointly optimized to enhance quality and discriminative of spot features for downstream tasks (Fig. 1). Specifically, AlignDG first learns spot features from the constructed networks using the graph auto-encoder (GAE), then aligns slices by simultaneously considering feature and structure consistency of spots across slices, where self-supervised learning is employed to further improve quality of features.

Attributed multi-layer network construction

The raw data of ST slices are preprocessed using SCANPY [47] and Seurat [48], where the count matrix undergoes normalization, logarithmic transformation, and scaling. Genes expressed in less than 10 cells are filtered out, and the top 10,000 highly variable genes are remained for downstream analysis.

Each ST slice containing n spots and m genes, is represented by an expression profile $X = [\mathrm{x}_1, \ldots, \mathrm{x}_n] \in \mathbb{R}^{m\times n}$ and a spatial coordinate profile $Y = [\mathrm{y}_1, \ldots, \mathrm{y}_n] \in \mathbb{R}^{2\times n}$. AlignDG constructs an attributed network $G = (V, E, X)$ for each slice by defining spots as vertices, the Euclidean distances between spot coordinates as edge weights, and spot expression profiles as vertex attributes. The K-nearest neighborhood (KNN) algorithm is employed to construct network, and the number of neighbors for each vertex varies across different platforms according to Ref. [49]. The topological structure of the attributed network G is represented by an adjacency matrix $W \in R^{n\times n}$,where the element w_{ij} denotes the weight of the edge connecting the i-th and j-th spot. Notice that variables with superscripts denote quantities corresponding to specific slices, i.e., $G^{[i]} = (V^{[i]}, E^{[i]}, X^{[i]})$, represents the attributed network for the i-th ST slice, where $V^{[i]}$, $E^{[i]}$, and $X^{[i]}$ are the set of spots, the set of edges, and the spot feature matrix, respectively.

Feature learning with graph model

AlignDG learns spot features by preserving both the intrinsic structure of the attribute matrix and topological structure of the graph using a graph attention auto-encoder (GAT) [50]. Specifically, the graph attention mechanism adaptively determines the influence of neighboring spots, thereby mitigating the impact of dropout events and noise in expression profiles.

AlignDG extracts features of spots using encoder of GAT, where output of the l-th layer of encoder corresponds to feature matrix $Z^{(l)} = [\mathrm{z}_1^{(l)}, \ldots, \mathrm{z}_n^{(l)}]$. $Z^{(l)}$ is calculated as

$$\mathrm{z}_i^{(l)} = \begin{cases} \mathrm{x}_i, & if \quad l = 0, \\ \sigma(\sum_{j\in\mathcal{N}_i} \alpha_{ij}^{(l)} B^{(l)} z_j^{(l-1)}), & if \quad l \in [1, \iota-1] \\ \sigma(B^{(\iota)} z_i^{(\iota-1)}), & if \quad l = \iota, \end{cases} \tag{1}$$

where $\mathcal{N}_i$ denotes set of neighbors of the i-th spot, $\sigma(\cdot)$ is a nonlinear activation function, $B^{(l)}$ represents the trainable weight matrix at the l-th layer, and $\alpha_{ij}^{(k)}$ denotes the learned attention coefficient, respectively. And, AlignDG reconstructs expression profiles of slices with decoder of GAT, where output of the l-th layer of decoder corresponds to reconstructed expression $\hat{X}^{(l)} = [\hat{\mathrm{x}}_1^{(l)}, \ldots, \hat{\mathrm{x}}_n^{(l)}]$. And, $\hat{X}^{(l)}$ is computed as

$$\hat{\mathrm{x}}_i^{(l)} = \begin{cases} \sum_{j\in\mathcal{N}_i} \hat{\alpha}_{ij}^{(l-1)} \sigma(\hat{B}^{(l)} \hat{z}_j^{(l)}), & \text{if} \quad l \in [1, \iota-1], \\ \sigma(\hat{B}^{(0)} \hat{\mathrm{x}}_i^{(0)}), & \text{if} \quad l = 0, \end{cases} \tag{2}$$

where $\hat{\mathrm{x}}_i^{(0)} = z_i^{(l)}$ is input of decoder, and $\hat{\alpha}_{ij}^{(l)} = \alpha_{ij}^{(l)}$ are the attention coefficients shared by encoder and decoder, respectively. AlignDG learns features of spots by minimizing the reconstruction loss, i.e.,

$$\mathcal{O}_{rec} = \|X - \hat{X}\|, \tag{3}$$

where $\|X\|$ is the Frobenius norm of matrix X, i.e., $\sqrt{\sum_{ij} x_{ij}^2}$.

Alignment of distant ST slices

AlignDG adopts optimal transport [39, 51] to align ST slices by preserving the local geometry of slices. This process generates a probabilistic coupling matrix that quantifies the correspondence likelihood between spots across slices.

Given two slices $\mathcal{S}^{[1]}$ and $\mathcal{S}^{[2]}$, containing $n^{[1]}$ and $n^{[2]}$ spots with marginal distributions $\mathrm{g}^{[1]}$ and $\mathrm{g}^{[2]}$, respectively, and a cost function $L : \mathcal{R} \times \mathcal{R} \to \mathcal{R}$, a four-order tensor $\mathrm{L} \in \mathcal{R}^{n^{[1]}\times n^{[2]}\times n^{[1]}\times n^{[2]}}$ is constructed with element $\mathrm{L}_{ijkl} = L(\mathcal{S}^{[1]}, \mathcal{S}^{[2]})$. According to Ref. [51], the Gromov-Wasserstain (GW) problem between a pair of ST slices is formulated as a minimization problem, i.e.,

$$\mathcal{O}(\mathcal{S}^{[1]}, \mathcal{S}^{[2]}) = \sum_{ijkl} L(\mathcal{S}^{[1]}, \mathcal{S}^{[2]}) \Gamma_{ij} \Gamma_{kl}, \tag{4}$$

where Γ is the coupling matrix defined as $\Pi(\mathrm{g}^{[1]}, \mathrm{g}^{[2]}) = \{\Gamma \in \mathcal{R}_+^{n^{[1]}\times n^{[2]}} : \Gamma 1_{n^{[2]}} = \mathrm{g}^{[1]}, \Gamma' 1_{n^{[1]}} = \mathrm{g}^{[2]}\}$, and 1_n denotes an n-dimensional vector with all elements as 1, respectively. By integrating features of spots Z and topological structure of the attributed network W from each slice, i.e., $\mathcal{S} = (Z, W, \mathrm{g})$, Eq.(4) can be extended to the Fused Gromov-Wasserstein (FGW) [51], which is formulated as

$$\mathcal{O}(\mathcal{S}^{[1]}, \mathcal{S}^{[2]}) = \sum_{ijkl} L_W(W^{[1]}, W^{[2]}) \Gamma_{ij} \Gamma_{kl} + \beta \sum_{ij} L_Z(Z^{[1]}, Z^{[2]}) \Gamma_{ij}, \tag{5}$$

where parameter $\beta \geq 0$ controls the relative importance of features of spots, and L_Z and L_W are the cost functions for features and topological structure of spots, respectively.

While several algorithms [33, 39] adopt the FGW formulation in Eq. (5) to perform alignment of ST slices, they present two critical limitations. First, Eq. (5) is applicable only to balanced samples, i.e., slices are global similar or replicates of the same tissue, which usually deviates from the expectation because of technical constraints and array placement. Consequently, these algorithms fail to align distant ST slices as shown in Fig. 1A. Second, most existing algorithms first fix cost functions L_W and L_Z, and then perform slice alignment. In this case, these algorithms separate intra-similarity within slices and alignment of slices,resulting in an undesirable performance.

To address the first unbalanced optimal transport problem, AlignDG introduces unbalanced transport to handle

distant slices, i.e., $\Gamma 1_{n^{[2]}} = \mathrm{g}^{[1]}$ and $\Gamma^{'} 1_{n^{[1]}} = \mathrm{g}^{[2]}$. On the basis of equivalence of mutual information [45, 52], AlignDG relaxes these equality constraints by incorporating mutual information terms. Accordingly, the objective function of unbalanced optimal transport in AlignDG is reformulated as

$$\begin{aligned}\mathcal{O}(\mathcal{S}^{[1]}, \mathcal{S}^{[2]}) = &\sum_{ijkl} L_W(W^{[1]}, W^{[2]})\Gamma_{ij}\Gamma_{kl} + \beta \sum_{ij} L_Z(Z^{[1]}, Z^{[2]})\Gamma_{ij} \\ &+ \alpha_1 I(\Gamma 1_{n^{[2]}}, \mathrm{g}^{[1]}) + \alpha_2 I(\Gamma^{'} 1_{n^{[1]}}, \mathrm{g}^{[2]}),\end{aligned} \tag{6}$$

where α_1, $\alpha_2 > 0$ are hyperparameters determining the penalties for deviation in the marginal distributions of ST slices.

To address the second limitation regarding the fixed cost functions, AlignDG automatically optimizes the cost function $L_Z(Z^{[1]}, Z^{[2]})$ with joint learning, as demonstrated in Fig. 1B. Furthermore, to accelerate the optimization of Eq. (6), we introduce a low-rank approximation of the optimal transport plan Γ, and derive the corresponding optimization rules (Additional file 1: Section 1.1).

Self-supervised learning

AlignDG improves quality of spot features by leveraging both topological structure of the attributed multi-layer networks and alignment of slices with self-supervised learning. Specifically, by treating each spot in slice $\mathcal{S}^{(1)}$ as an anchor, AlignDG selects the top k spots from $\mathcal{S}^{(2)}$ with the highest mapping probability from Γ as positive pairs, and randomly samples k spots from slice $\mathcal{S}^{(1)}$ as negative pairs. Let $\varrho = \{(C_{anc}, C_{pos}, C_{neg})\}$, where each object denotes a triplet consisting of an anchor, a positive, and a negative spot. AlignDG employs self-supervised learning to enforce positive pairs to be close in feature space while pushing negative pairs apart. The self-supervised loss is formulated as:

$$\mathcal{L}_{self} = \frac{1}{n_\varrho} \sum_{\varrho} [s(\mathrm{z}_{anc}, \mathrm{z}_{neg}) - s(\mathrm{z}_{anc}, \mathrm{z}_{pos}) + \xi]_+, \tag{7}$$

where n_ϱ denotes the total number of triplets, $[x]_+ = max(x, 0)$, and $s(\cdot)$ measures the similarity between features of spots, respectively.

AlignDG joins self-supervised learning and feature learning as

$$L = L_{rec} + \eta L_{self}, \tag{8}$$

where the hyperparameter η controls the relative importance of self-supervised learning term (parameter selection and analysis are presented in Additional file 1).

3D Reconstruction of tissue architecture

Given multiple consecutive ST slices $\{\mathcal{S}^{[1]}, \ldots, \mathcal{S}^{[m]}\}$, AlignDG provides two strategies for 3D tissue reconstruction, i.e., pairwise- and reference-based strategy. The pairwise-based strategy aligns each consecutive slice pair (i.e., $\mathcal{S}^{[1]} \leftrightarrow \mathcal{S}^{[2]}$, , $\mathcal{S}^{[m-1]} \leftrightarrow \mathcal{S}^{[m]}$), eventually processes all slices for 3D architecture of tissues. And, the reference-based strategy selects one slice $\mathcal{S}^{[r]}$ as reference, and aligns all other slices to it (i.e., $\mathcal{S}^{[1]} \leftrightarrow \mathcal{S}^{[r]}$, , $\mathcal{S}^{[m]} \leftrightarrow \mathcal{S}^{[r]}$).

For each pair of ST slices, AlignDG transforms spatial coordinates of spots into a common coordinate system by using the weighted procrustes analysis [53, 54]. Specifically, given alignment matrix Γ between slice $\mathcal{S}^{[1]}$ and $\mathcal{S}^{[2]}$, AlignDG estimates rotation matrix R and translation vector T to minimize weighted distances between aligned spots across slices as

$$\min_{R,T} \|\Gamma^{'}(Y^{[1]} - RY^{[2]} - T)\|^2, \quad \text{s.t. } R^{'}R = I. \tag{9}$$

Algorithm performance metrics

Several quantitative metrics are employed to evaluate the performance of all algorithms. Specifically, pairwise alignment accuracy (PAA) and spot-to-spot matching ratio (SMR) [55] are utilized to evaluate the alignment performance across ST slices. Concurrently, integration local inverse Simpson's index (iLISI) and cell type local inverse Simpson's index (cLISI) [26] are selected to evaluate performance of algorithms for removing batch effect of ST slices, and adjusted rand index (ARI) [56] is selected to evaluate performance of algorithms for identifying spatial domains within ST slices.

Specifically, given alignment matrix Γ (Γ_{ij} denotes the probability that the i-th spot in $\mathcal{S}^{[1]}$ aligns with the j-th spot in $\mathcal{S}^{[2]}$), PAA [55] is defined as

$$PAA = \frac{\sum_{i \in \mathcal{S}^{[1]}} \delta(c_i^{[1]}, c_{j^*})}{n^{[1]}}, \tag{10}$$

where $c_i^{[1]}$ is the cell type of the i-th spot in $\mathcal{S}^{[1]}$, $j^* = \arg\max_j \Gamma_{ij}$, and $\delta(c_i, c_j)$ denotes Kronecker delta function, which equals 1 if $c_i = c_j$, and 0 otherwise. SMR [55] is formulated as

$$SMR = \frac{n_1}{|\mathcal{U}|} \tag{11}$$

where $\mathcal{U} = \{j^* | j^* = \arg\max_j \Gamma_{ij} \text{ for } i \in \mathcal{S}^{[1]}\}$, and $|\mathcal{U}|$ denotes the cardinality of $\mathcal{U}$, i.e., the number of elements in $\mathcal{U}$.

On spatial domain identification issue, given spatial domains identified by algorithms P and ground truth domains P^* of slice $\mathcal{S}$ with n spots, ARI [56] is defined as

$$ARI(P^*,P)=\frac{\sum_{ij}\binom{n_{ij}}{2}-\left[\sum_i\binom{|C_i|}{2}+\sum_j\binom{|C_j|}{2}\right]/\binom{n}{2}}{\frac{1}{2}\left[\sum_i\binom{|C_i|}{2}+\sum_j\binom{|C_j|}{2}\right]-\left[\sum_i\binom{|C_i|}{2}+\sum_j\binom{|C_j|}{2}\right]/\binom{n}{2}}, \quad (12)$$

where n_{ij} is the number of spots overlapped by the i-th cluster in P^* and j-th cluster in P, and $|C_i|$ is the number of spots in cluster C_i.

Clustering and visualization

Based on the learned spot features, AlignDG employs Leiden algorithm [57] (implemented by SCANPY [47] package) to derive cluster assignments, where each cluster corresponds to a distinct spatial domain (the number of clusters is determined by PhenoGraph [58]). The uniform manifold approximation and projection (UMAP) [59] algorithm is selected to visualize the learned features.

Identification and functional analysis of differentially expressed genes

AlignDG performs differential expression analysis of genes for each spatial domain by using Wilcoxon rank-sum test (implemented in SCANPY package [47]). Genes expressed in more than 80% of cells/spots in each domain, with a fold change $\geq$ 1.5 and an adjusted FDR $\leq$ 0.05, are selected as differentially expressed genes (DEGs). The filtered DEGs are then serve as input for gene ontology enrichment analysis, which is conducted with clusterProfiler [60]. Enriched functional terms with -log10(adjusted *P*-value) are plotted.

Data cohorts

Human dorsolateral prefrontal cortex dataset

The human dorsolateral prefrontal cortex (DLPFC) dataset [61] is profiled using the 10× Genomics Visium platform. It consists of twelve slices, where each slice contains 3,460-4,789 spots and 33,538 genes. Spots of each slice are manually annotated into six cortical layers and white matter (WM) on the basis of the canonical marker genes.

Mouse hypothalamic preoptic dataset

The mouse hypothalamic preoptic region dataset is profiled with MERFISH platform [62], which consists of eleven slices, and each one contains 6,813 10,796 cells and 161 genes. Cells of each slice are manually annotated into sixteen cell types, including Astrocyte, Inhibitory, Pericyte, Ambiguous, Endothelial 1, Excitatory, OD Immature 1, OD Immature 2, Microglia, OD Mature 2, OD Mature 1, Endothelial 3, OD Mature 3, OD Mature 4, Endothelial 2, and Ependymal.

Mouse embryo datasets

To benchmark performance of AlignDG for alignment of ST slices across various platforms and developmental stages, two mouse embryo datasets are selected. Specifically, the first dataset is profiled using seqFISH [63] at embryonic day 8.75 (E8.75), containing 11,529 cells and 351 genes, and all cells are manually annotated into 21 major tissues or organs. The second dataset is a spatiotemporal mouse embryo dataset spanning embryonic days from 9.5 to 16.5 (E9.5–16.5.5), consisting of eight slices at distinct developmental stages. Each slice contains 5,913 121,767 spots and 25,568 genes. All spots are manually annotated into 45 tissues or organs.

Human cancer datasets

To benchmark the performance of AlignDG on cross-platform cancer slice alignment, we first employ human breast cancer slices co-assayed using 10× Genomics Visium and Xenium. The Visium slice contains 3,841 spots and 17,820 genes, whereas the Xenium slice [64] includes 100,642 cells and 313 genes. Notably, triple-positive cells were annotated in the Xenium slice but not in the Visium slice. To further evaluate the potential of AlignDG in aligning slices from different cancer types, we additionally employ one breast cancer slice and one ovarian cancer slice profile using Visium platform. The additional breast cancer slice contains 3,798 spots and 18,601 genes, while the ovarian cancer slice contains 3,493 cells and 15,832 genes

Mouse olfactory bulb datasets

Two mouse olfactory bulb datasets are employed for experiments, where the first one is profiled using Slide-seqV2 platform [5], containing 20,139 cells and 21,220 genes. And, the second dataset is generated using Stereo-seq platform [6], consisting of 19,109 spots and 14,376 genes.

Axolotl brain regeneration dataset

The axolotl brain regeneration process profiled using Stereo-seq platform [6] is selected to validate performance of algorithms for the identification of spatiotemporal patterns, which contains seven slices across different stages ranging from 2 to 60 days post-injury (DPI). Each slice has 8,192 10,964 spots, and all spots are manually annotated into 26 cell types to investigate cell migration during regeneration.

Mouse brain datasets

One normal mouse hippocampus slice and one Alzheimer's disease (AD) related hippocampus slice are selected for experiments, where the normal hippocampus slice contains 13,583 spots and 19,653 genes, and the AD-related hippocampus slice contains 15,092 spots and 27,222 genes, respectively.

Results

Overview of AlignDG for distant slice alignment

Before presenting an overview of AlignDG, we first illustrate several typical scenarios involving the alignment of distant slices, such as non-consecutive slices of tissues, slices of developmental stages with a large gap, slices from distinct tissues, as well as slices under diverse experimental conditions (Fig. 1A). These scenarios are ubiquitous and inevitable in biological and medical fields, which cannot be effectively addressed by available state-of-the-art algorithms. And, the alignment of distant slices is particularly valuable, as it substantially reduces the number of ST slices required for integrative analysis, thereby alleviating experimental and financial burdens. Moreover, aligning distant slices across tissues or diseases can reveal potential biological insights that are undetectable through adjacent slice alignment. Thus, it is of great significance to perform distant slice alignment, forming the core rationale and motivation of this study. AlignDG is a network-based model for distant slice alignment, providing a novel strategy for analyzing ST data.

As shown in Fig. 1B, AlignDG consists of three components, i.e., attributed multi-layer network construction for multiple slices, feature learning using the graph attention auto-encoder model, and slice alignment with mutual information (Section Methods). AlignDG takes normalized expression profile and spatial coordinates of ST slices as input. On the network construction issue, it constructs spatial network of spots using K-nearest neighborhood (KNN), where Euclidean distances of spatial coordinates between spots define the edge weights, and expression profiles serve as spot attributes, thereby forming spot attributed multi-layer networks. Then, AlignDG employs a graph attention auto-encoder neural network to learn discriminative spot features, which projects attributed multi-layer networks into a shared latent space, thereby obtaining consistent spot features and mitigating inter-slice heterogeneity.

On the alignment of distant and unbalanced slices issue, AlignDG further employs optimal transport to obtain alignment probabilities across slices by simultaneously exploiting spatial proximity and transcriptional similarity of spot pairs across slices. Specifically, AlignDG handles transportation of unbalanced slices via minimizing mutual information, which evaluates correspondences of spots across slices in terms of distributions of features of spots, rather than features themselves. In this case, AlignDG provides a precise and robust way to model mapping between spot pairs for partial alignment between unbalanced slices. To further improve feature quality, AlignDG jointly learns spot features and slice alignments, where feature learning is guided by the alignment result. Additionally, a self-supervised learning strategy is introduced to improve feature discriminability by contrasting positive and negative spot pairs. Finally, AlignDG is formulated as a mutual information regularized Wasserstein optimization problem, which is effectively solved using mirror gradient descent (Section Methods, Additional file 1: Section 1.1 and 1.2). Furthermore, AlignDG addresses the alignment of distant and unbalanced ST slices, which cannot be fulfilled by baselines.

Benchmarking AlignDG with various simulated datasets

Three simulated datasets generated with Splatter [65] are selected to evaluate performance of algorithms. Dataset 1 maintains identical cell types and spatial coordinates across slices (Additional file 1: Fig. S1A), while Dataset 2 only preserves cell types with distant spatial coordinates (Additional file 1: Fig. S1B). Dataset 3 exhibits distinct cell compositions and spatial coordinates (Fig. 2A, Additional file 1: Fig. S1C). Twelve state-of-the-art algorithms, including Seurat [24], Harmony [26], PASTE [39], PASTE2 [33], STAligner [41], SLAT [43], SPACEL [38], CAST [37], Spateo [35], DeepST [11], GraphST [66], and Moscot [45], are selected as baselines. STalign [34] and SANTO [36] are excluded due to their inability to output the required spot-to-spot mappings across slices. PAA (pairwise alignment accuracy, higher PAA represents better performance) and SMR (spot-to-spot Matching Ratio, lower value denotes better performance) [55] are selected to measure performance of various algorithms (Section: Methods).

Parameter analysis indicates that AlignDG is quite robust for different hyperparameters, and under unbalanced conditions, the performance of AlignDG is correlated with overlap ratios between slices (Additional file 1: Section 1.3, Fig. S2-S3). Performance of different algorithms on Dataset 1 indicates that AlignDG achieves the best performance (Additional file 1: Fig. S4A) with PAA 0.960 and SMR 1.098, which outperforms baselines. STAligner is inferior to AlignDG because it fails to fully leverages spatial information, and PASTE2 inferior to PASTE as it is specifically designed for partial alignment of slices. These results demonstrate that AlignDG is promising for balanced and similar slices. Performance of various algorithms on Dataset 2 further shows that AlignDG also achieves the best performance with PAA of 0.956 and SMR of 1.111, followed by Moscot 0.952 and 1.116 (Additional file 1: Fig. S4B). Figure 2A visualizes slices of Dataset 3 (left), and alignment obtained by various algorithms (right), where cell types are labeled with different colors, and mapping of spot pairs is labeled with colors (sub-sampled to 150 alignment pairs for illustration, blue lines for correct alignment, and red for incorrect ones). Interestingly, AlignDG still achieves the best performance with PAA 0.858 and SMR 1.144, whereas

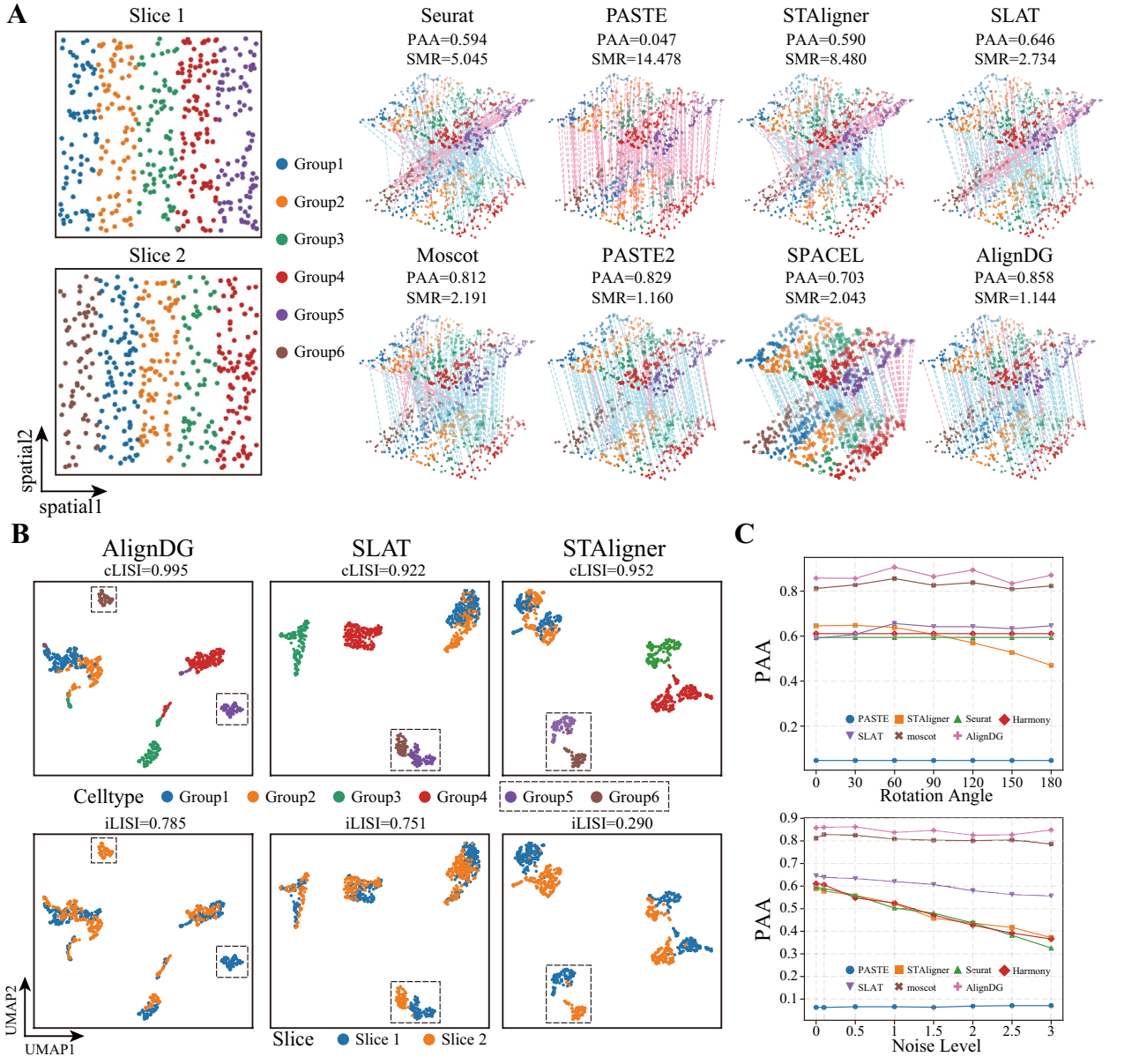

Fig. 2 Performance of various algorithms for slice alignment on various simulated datasets. **A** Visualization of slices with UMAP, where cell types are labeled with colors (left), and visualization of alignment obtained by various algorithms, where colors of cells correspond to cell types, and vertical lines connect aligned cell pairs (sub-sampled to 150 alignment pairs for a better illustration, blue for correct alignment and red for incorrect ones, right), **B** Visualization of cell types (top) and slices (bottom) after removing batch effect in Dataset 3, and **C** PAA of various algorithms for slice alignment by perturbing Dataset 3 with rotation (top) and noise (bottom), respectively

PAA and SMR of the best baseline PASTE2 is 0.829 and 1.160, respectively (Additional file 1: Fig. S4C).

These two slices of Dataset 3 share the common Group 1–4, while Group 5 and 6 are specific to slices 1 and 2 respectively. And, we select iLISI (integration Local Inverse Simpson's Index) and cLISI (cell type local inverse simpson's index) [26, 67], to measure performance of various algorithms for removing batch effect and discriminating slice-specific groups. Figure 2B (top panel) visualizes cell types with features learned by various algorithms, where AlignDG and STAligner can precisely separate Group 5 and 6. However, other baselines cannot fully discriminate them (surrounded by dashed squares, Fig. 2B and Additional file 1: Fig. S5). Notice that distance between these two groups of AlignDG is much larger than STAligner, demonstrating that AlignDG is more precise to characterize slice-specific groups than STAligner. Figure 2B (bottom panel) visualizes consistency of cell types from different slices in terms of features, where AlignDG (iLISI=0.785) effectively mixes cells with shared labels across slices in feature space and accurately discriminating Group 5 and 6, showing that

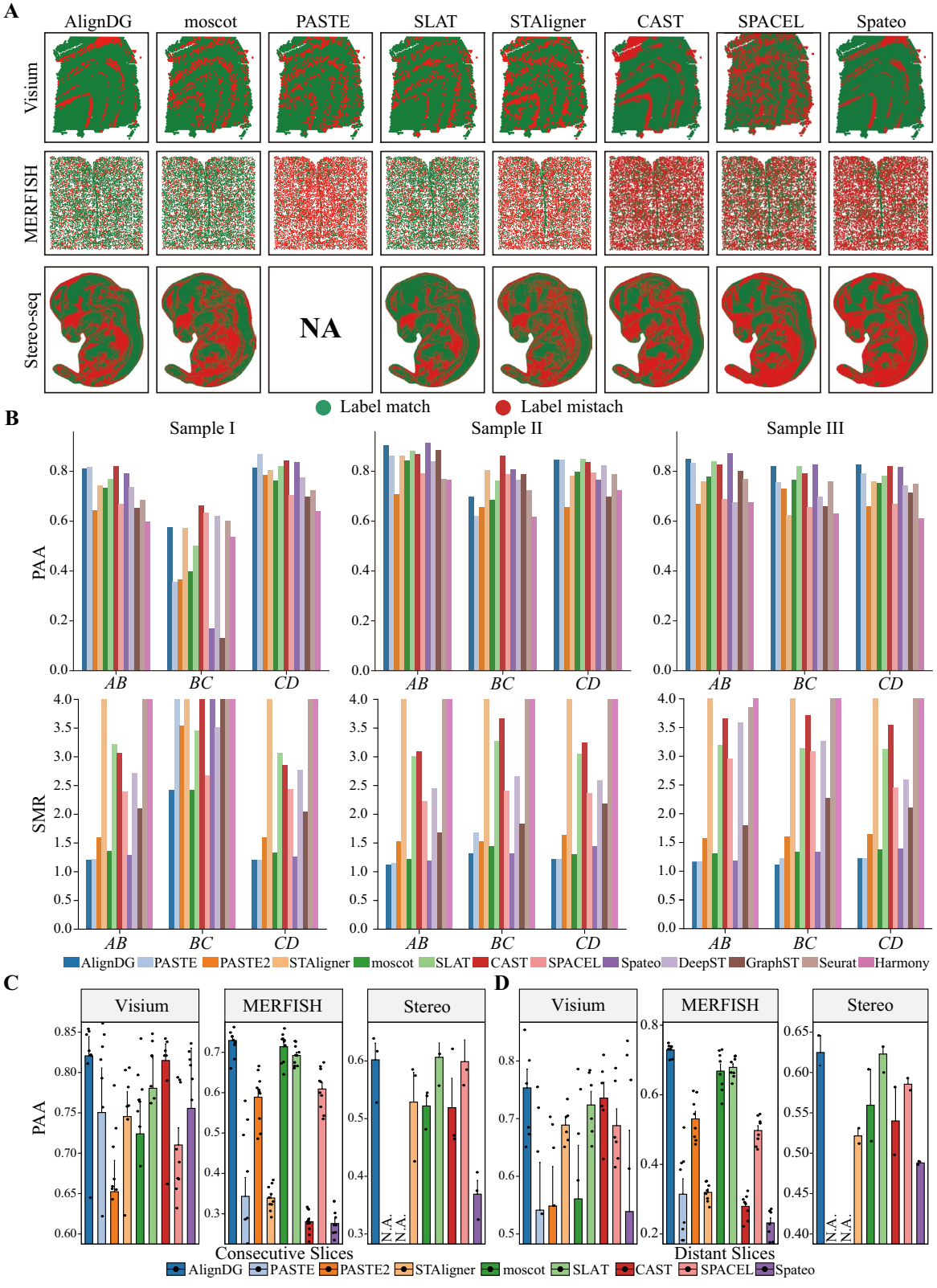

Fig. 3 (See legend on next page.)

(See figure on previous page.)

Fig. 3 Performance of algorithms for aligning adjacent and distant slices across various tissues. **A** Visualization of alignment results of different algorithms on the first slice of datasets generated by 10× Visium, MERFISH and Stereo-seq platform, where green denotes correct alignment for cell types and regions, and red for incorrect alignment for either of them (NA denotes no outputs), **B** Performance of algorithms for aligning consecutive slices of DLPFC dataset (denoted by *AB*, *BC*, and *CD*) in terms of PAA (top, high PAA indicates better performance) and SMR (bottom, lower value denotes better performance), and **C**/**D** PAA of algorithms on consecutive (non-consecutive) pairwise slices, where missing bar denotes no outputs, and error bars denotes mean and standard deviation

AlignDG precisely removes batch effect in slices while preserving underlying biological variation (Additional file 1: Fig. S5A-C). These results demonstrate that AlignDG learns discriminative features, providing a better way to characterize structure of these simulated datasets.

Moreover, we investigate the robustness of algorithms on Dataset 3 by introducing perturbations through both rotation of slices (at varying angles) and expression profile noise. Figure 2C (top) depicts how PAAs of various algorithms change as the rotation angle increases from 0 to 180 degree, where AlignDG achieves the best performance (PAA=0.869 ± 0.023, mean ± standard deviation), followed by Moscot (PAA=0.827 ± 0.016). And, Fig. 2C (bottom) describes how PAAs of various algorithms change as noise level increases from 0 to 3, where PAA of AlignDG is 0.845 ± 0.013, followed by Moscot with PAA 0.808 ± 0.014. These results confirm the superiority of AlignDG over baselines in both accuracy and robustness, demonstrating that the joint learning of features and alignment is promising. Two reasons explain why AlignDG outperforms baselines. First, it makes use of expression and topological structure of spatial network of spots, thereby bridging complementary information of transcriptomics and spatial proximity. Second, AlignDG joins feature learning, alignment, and self-supervised learning, which enhances quality and discriminative of spot features, thereby providing a more comprehensive strategy to model consistency of slices.

We also evaluate the performance of all these algorithms on synthetic datasets without alignable regions, and find that AlignDG effectively avoids over-fitting, whereas baselines exhibit high false-positive rates (Additional file 1: Fig. S6). Finally, the ablation study further confirms that all components of AlignDG are essential because removing either of these components decreases performance, proving conciseness of the proposed algorithm (Additional file 1: Fig. S7).

AlignDG significantly improves alignment accuracy of adjacent and distant slices across tissues

Except for simulated datasets, we further evaluate performance of AlignDG with three biological datasets representing different tissues and generated from different platforms, including DLPFC (human dorsolateral prefrontal cortex, 10× Visium) [61], HPC (mouse hypothalamic preoptic region, MERFISH) [68], and mouse embryo (Stereo-seq) [69]. The DLPFC includes twelve slices, HPC includes eleven slices, and mouse embryo includes four slices, respectively.

Figure 3A illustrates the alignment results of different algorithms on the first two slices of these three datasets, where correctly aligned regions are labeled in green, otherwise red. We observe that AlignDG outperforms baselines on the DLPFC and MERFISH dataset, and has a similar performance with SLAT. Specifically, AlignDG performs best on the Visium DLPFC and MERFISH HPC dataset, and it is only surpassed by SLAT on the Stereo-seq mouse embryo dataset. In details, the PAA of various algorithms on the DLPFC dataset is 0.851 (AlignDG), 0.779 (Moscot), 0.832 (PASTE), 0.839 (SLAT), 0.759 (STAligner), whereas that for HPC dataset is 0.730 (AlignDG), 0.729 (Moscot), 0.208 (PASTE), 0.693 (SLAT), 0.324 (STAligner), respectively. The PAA scores of all algorithms on Stereo-seq dataset is worse than that on 10 × Visium and MERFISH because tissues in embryo are more complicated than those in others (Additional file 1: Fig. S8-S9). Notice that PASTE and its variants failed to address Stereo-seq datasets because it is time-/space- consuming, which limits its application to large-scale datasets. AlignDG achieves the best performance across all three datasets as a whole, demonstrating that the proposed joint graph learning model is precise in aligning slices from various platforms.

The DLPFC dataset is originated from three individuals (labeled I, II and III), each comprising four slices (labeled *A*, *B*, *C* and *D*). Interestingly, the four slices of each individual include both adjacent and distant slice pairs, i.e., the first (last) two slice pairs *AB* (*CD*) are directly adjacent (10μm apart), whereas the middle slice pair *BC* is distant (300 μm apart) (Additional file 1: Fig. S10). Hence, DLPFC naturally serves as a benchmark to validate performance of various algorithms for aligning adjacent and distant slices. Figure 3B reports performance of different algorithms on pairwise alignments of consecutive slices from the same sample, measured by PAA (top) and SMR (bottom). AlignDG achieves the best performance for 3 of the 9 pairwise alignments in terms of PAA, achieving high alignment accuracy for adjacent pairs. Notably, AlignDG, STAligner and SLAT are much better than baselines for distant slice pairs (middle pair *BC*), whereas performance of PASTE and Moscot declines dramatically. Seurat and Harmony are inferior to others, showing that spatial information is necessary for slice alignment. Furthermore, AlignDG is more robust than baselines

across all pairwise alignments, whereas STAligner, Seurat and Harmony are sensitive to perturbation of dataset, particularly for the distant slice alignment. For example, PAA of STAligner for *BC* pair in Sample II is 0.806, and decreases to 0.623 in Sample III, demonstrating that spatially-aware embedding only is insufficient to precisely align distant slices. Surprisingly, AlignDG achieves the best performance for all slice pairs in terms of SMR, demonstrating that AlignDG is promising for aligning slices of datasets generated by Visium (Fig. 3B bottom).

Then, we investigate performance of different algorithms for aligning consecutive slices generated by various platforms. Figure 3C summarizes the PAA results for all datasets, where AlignDG achieves the best performance on both the Visium DLPFC and MERFISH HPC datasets in terms of PAA and SMR. For the Stereo-seq mouse embryo dataset, AlignDG is superior to baselines, only inferior to SLAT in terms of PAA. However, it outperforms all these baslines in terms of SMR (Additional file 1: Fig. S11). In details, PAA and SMR of various algorithms on DLPFC is 0.822 ± 0.093 and 1.340 ± 0.388 (AlignDG), whereas those are 0.764 ± 0.122 and 1.458 ± 0.345 for Moscot, 0.816 ± 0.156 and 1.653 ± 1.116 for PASTE, and 0.820 ± 0.106 and 3.172 ± 0.129 for SLAT, respectively. On the MERFISH HPC dataset, STAligner, PASTE, CAST and Spateo perform the worst with PAAs of 0.339 ± 0.028, 0.343 ± 0.140, 0.281 ± 0.027, and 0.276 ± 0.036, respectively. In contrast, AlignDG achieves the best performance with PAA of 0.735 ± 0.016, demonstrating that the proposed algorithm also applicable to MERFISH data. And, we obverse that AlignDG also achieves the best SMR (1.294 ± 0.107) for all pairs of slices, further demonstrate the robustness of the proposed algorithm. STAligner, which ignores spatial information for slice alignment, resulting in undesirable performance of PAA and SMR, while AlignDG, SLAT, and Moscot achieve better performance by leveraging spatial information for alignment. To investigate why PASTE and STAligner achieve poor performance, we visualize the coupling matrix among cell types, where rows correspond to cell types predicted by various algorithms, columns denote ground truth cell types, and elements are number of matches within the corresponding predicted and truth cell type pairs (Additional file 1: Fig. S12). We find that both STAligner and PASTE fail to align rare cell types. For instance, PASTE and STAligner incorrectly align *OD mature 3* and *OD mature 4* to *Astrocyte*, *Inhibitory*, suggesting that meta-structure of spots in slices is also critical for slice alignment. AlignDG joints learning spot features and alignment, where meta-information in alignment serves as prior information to enhance quality of features.

In addition to the alignment of adjacent slices, we also perform distant slice alignment, i.e., pairwise non-consecutive slice alignment, using all three datasets (Fig. 3D, Additional file 1: Fig. S13). AlignDG outperforms all these baselines in distant alignment. For example, PAA and SMR of AlignDG is 0.801 and 1.268 (*AC* in DLPFC), 0.731 and 1.246 (*S1-S4* in HPC), 0.653 and 1.511 (*S1-S3* Stereo-seq), whereas that of STAligner is 0.703 and 7.094 (*AC* in DLPFC), 0.325 and 7.959 (*S1-S4* in HPC), 0.531 and 3.664 (*S1-S3* Stereo-seq), respectively. Performance of all these algorithms for distant alignment on these three datasets are summarized in Fig. 3D, where AlignDG also achieves the best performance for both PAA and SMR, demonstrating that it effectively overcoming unbalanced alignment for distant slices (Additional file 1: Fig. S11). In contrast, none of the baseline algorithms can accurately align distant slices, suggesting the superiority of the proposed network-based model for distant alignment as it simultaneously addresses unbalance, discriminative and independence assumption in adjacent alignment.

We also evaluate performance of different algorithms on removing batch effect across slices (Additional file 1: Fig. S14A-B), where AlignDG achieves the best performance (iLISI = 0.915 and cLISI = 0.964), demonstrating effective preservation of biological variability while minimizing technical biases. In addition, we evaluate the performance of different algorithms for the identification of spatial domains, where AlignDG and STAligner obtain the best performance (Additional file 1: Fig. S14C). The computational efficiency of these algorithms is also conducted in terms of running time by varying the number of cells from 3,200 to 102,400 (Additional file 1: Fig. S15), where AlignDG and Moscot are the only spatially-aware algorithms capable of handling slices with > 100,000 cells. Overall, AlignDG outperforms baselines for aligning adjacent and distant slices with high computational efficiency for large-scale ST data.

AlignDG improves alignment and integration of distant slices across different platforms

Evidence [70] suggests that integrating analysis of slices generated from different platforms leverages complementary advantages, enabling super-resolution reconstruction of large tissues, allowing accurately prediction of gene expression at near-single-cell spatial resolution. Here, we validate performance of AlignDG with three additional datasets of the same tissue across different platforms, including the mouse olfactory bulb (OFB) slices sequenced by Slide-seq V2 and Stereo-seq, whole mouse embryo slices sequenced by seqFISH and Stereo-seq, and human breast cancer slices co-assayed by 10× Visium and Xenium, respectively. Since ground-truth alignments are unavailable for these datasets, we assess performance of algorithms through batch-effect removal and cross-slice domain annotation mapping. PASTE,

PASTE2, Spateo and Moscot are excluded as they fail to remove batch effect, and SPACEL, GraphST, DeepST are also excluded for their inability to integrate ST slices with significant difference.

The mouse olfactory bulb dataset is generated by Slide-seqV2 [5] and Stereo-seq platform [6] from the same tissue at different spatial resolutions (Fig. 4A), and these slices are annotated with DAPI-stained image [71] and Allen Mouse Brain Atlas [72], where the accessory olfactory bulb (AOB) and granular layer of the accessory olfactory bulb (AOBgr) are Slide-seqV2-specific. Since alignment of various slices elucidates the conserved spatial domains across slices, we hypothesize that this information can facilitate batch-effect removal and the identification of spatial domains, which is fulfilled with self-supervised learning in AlignDG by enforcing features of matched spots across slices are consistent. Figure 4B visualizes different slices and spatial domains identified by AlignDG, where top panel is colored for platforms (blue: Stereo-seq, orange: Slide-seq V2) and bottom panel for spatial domains. The embeddings obtained by AlignDG are consistently overlapped, demonstrating

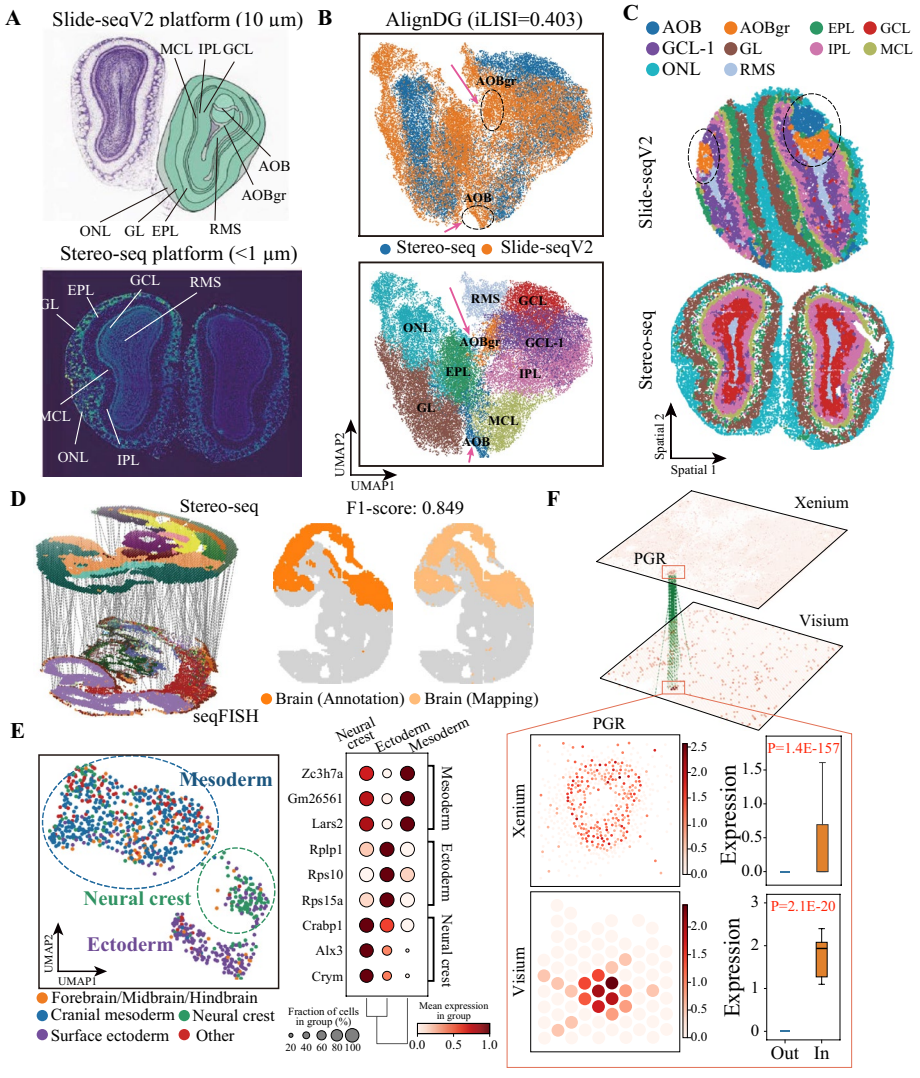

Fig. 4 AlignDG improves alignment and integration of distant slices of various datasets across different platforms. **A** Laminar organization of mouse olfactory bulb annotated by Allen Mouse Brain Atlas (top) and DAPI-stained image (bottom), which are generated by Slide-seq V2 and Stereo-seq platform, respectively. **B** UMAP visualization of embedding of spots obtained by AlignDG. Spots are colored with different colors, where blue corresponds to Stereo-seq slice and orange to Slide-seq V2, respectively (top). And, visualization of spatial domains identified by AlignDG (bottom), where platform-specific domains are identified (red arrow and elliptical black dashed lines). **C** Visualization of spatial domains identified by AlignDG. **D** Visualization of alignment results obtained by AlignDG on the mouse embryo slices generated by seqFISH and Stereo-seq platforms (left), and visualization of the ground truth brain region (middle) and predicted by AlignDG with alignment (right, F1-score=0.849). **E** Visualization of *Neural crest* region in Stereo-seq and corresponding aligned cell types in seqFISH, where dashed circles are manual annotation with bio-marker genes. **F** Alignment of breast cancer slices co-assayed by Xenium and Visium platforms obtained by AlignDG (top), and visualization of heatmap and spatial distribution of expression of biomarker gene *PGR* inside and outside of matched regions (two-sided Student's t-test for significance)

that batch effect is effectively removed, whereas Seurat fails to characterize and remove batch effect in slices since overlapping is limited (Additional file 1: Fig. S16A). Notably, only AlignDG and STAligner successfully identify the slice-specific structure AOB and AOBgr (dashed circle in Fig. 4B, Additional file 1: Fig. S16B), whereas all other baselines fail to identify these domains. These results demonstrate that AlignDG and STAligner effectively remove batch effects while preserving slice-specific structures. In contrast, other baselines exhibit over-correction by sacrificing specific structures of slices (Additional file 1: Fig. S16A). By visualizing the identified spatial domains on both slices, we confirm that AOB and AOBgr are slice-specific (dashed circle in Fig. 4C), which cannot be recovered by other algorithms (Additional file 1: Fig. S16B and C), demonstrating that AlignDG also accurately aligns slices at the cellular and sub-cellular resolution.

Then, we evaluate the performance of AlignDG with the shape-like whole mouse embryo slices profiled by seqFISH and Stereo-seq, which are unbalanced, i.e., seqFISH slice contains over 10,000 cells and 350 genes [63, 73], Stereo-seq slice contains 5,000 spots and over 20,000 genes [69]. Meanwhile, cell types of slices also differ greatly, where the number of cell types is 21 and 11 for seqFISH and Stereo-seq slice, respectively (Additional file 1: Fig. S17A and B). Interestingly, AlignDG and SLAT precisely capture cell-type transfer across platforms, which is critical for understanding cellular states transitions. For example, *Neural crest* cells in Stereo-seq slice are aligned to five major cell types in seqFISH slice (Fig. 4E, Additional file 1: Fig. S17C), thereby refining cell-type annotations that are further validated by known biomarker genes (Additional file 1: Fig. S17D-E). Notably, slices from these two platforms also differ in spatial structure with substantial non-rigid deformations, where only AlignDG, STAligner and SLAT track these spatial variations. Visualization of aligned brain cells across slices also demonstrate that AlignDG achieves higher accuracy than baseline methods in aligning cell types, as quantified by multiple metrics, including F1-score, false positive rate, ARI and NMI (Fig. 4D, Additional file 1: Fig. S18 and S19A, Methods section). Further analyses of batch-effect removal and spatial domain identification confirm that AlignDG is promising for processing slices generated by seqFISH and Stereo-seq platform (Additional file 1: Fig. S19B-D).

Moreover, human breast cancer slices co-assayed by 10× Visium and Xenium are selected with various genomic coverage and spatial resolutions, where Xenium slice covers more than 100,000 cells with 313 genes, and Visium slice contains 3,841 spots covering over 20,000 genes. AlignDG aligns the shared spatial regions across slices, such as invasive region and the ductal carcinoma in situ (DCIS) region, showing that AlignDG accurately identifies shared spatial structures of slices with different coverage and resolutions (Additional file 1: Fig. S20). Notably, the rare triple-positive breast tumor cells manually annotated in Xenium, rather than Visium (Additional file 1: Fig. S20A), is only captures by AlignDG and SLAT, whereas others fail to identify it (Fig. 4E top panel, Additional file 1: Fig. S21). Furthermore, differential expression analysis for triplet-positive cells identify 25 differentially expressed genes (DEGs), where 18 of these 25 DEGs are previously confirmed as established biomarkers for triple-positive breast cancer as supported in the literature. For example, as one of three top DEGs, *PGR* is significantly upregulated within the matched spatial domain (Fig. 4E bottom panel, two-sided Student's t-test, p=1.4E-157 for Xenium, and p=2.1E-20 for Visium). These results show that AlignDG not only accurately aligns spots across slices, but also effectively maps rare spatial domains of slices across platforms.

Overall, AlignDG effectively aligns distant slices across different platforms, which not only accurately removes batch effects, but also captures cross-platform label transfer of cell types, thereby bridging barcode- and imaging-based ST technologies.

AlignDG accurately aligns consecutive and non-consecutive spatial-temporal slices

Spatiotemporal spatial transcriptomics datasets offer unprecedented opportunities to investigate developmental trajectories and transitional processes across various stages of tissues, and two spatiotemporal datasets generated by Stereo-seq [6, 69] are selected to investigate whether AlignDG can effectively align continuous and non-continuous spatiotemporal slices, and track development of tissues.

Mouse embryo dataset [69] across 8 time points from E9.5 to E16.5 is selected, where each time point corresponds to a slice annotated with different cell types and organs (Additional file 1: Fig. S22A). To investigate whether AlignDG precisely tracks development of majors organs, such as *brain*, *heart*, *liver* and *lung*, we perform alignment for each of two continuous slices, and utilize these subsequent alignment results to track development of organs (Additional file 1: Fig. S22B-C). Figure 5A visualizes development of four main organs from E9.5 to E16.5 tracked by AlignDG (middle) and Moscot (bottom), where organs predicted by AlignDG are highly consistent with annotation at each time point (top). Specifically, F1-score of *heart* predicted by AlignDG is 0.811 ± 0.080, whereas that of Moscot is 0.694 ± 0.096, demonstrating that AlignDG is more precise to track evolving spatial domains in spatial-temporal slices. Except for *heart*, AlignDG accurately recapitulates development of all organs (*brain*: F1-score=0.786 ± 0.100, and *liver*:

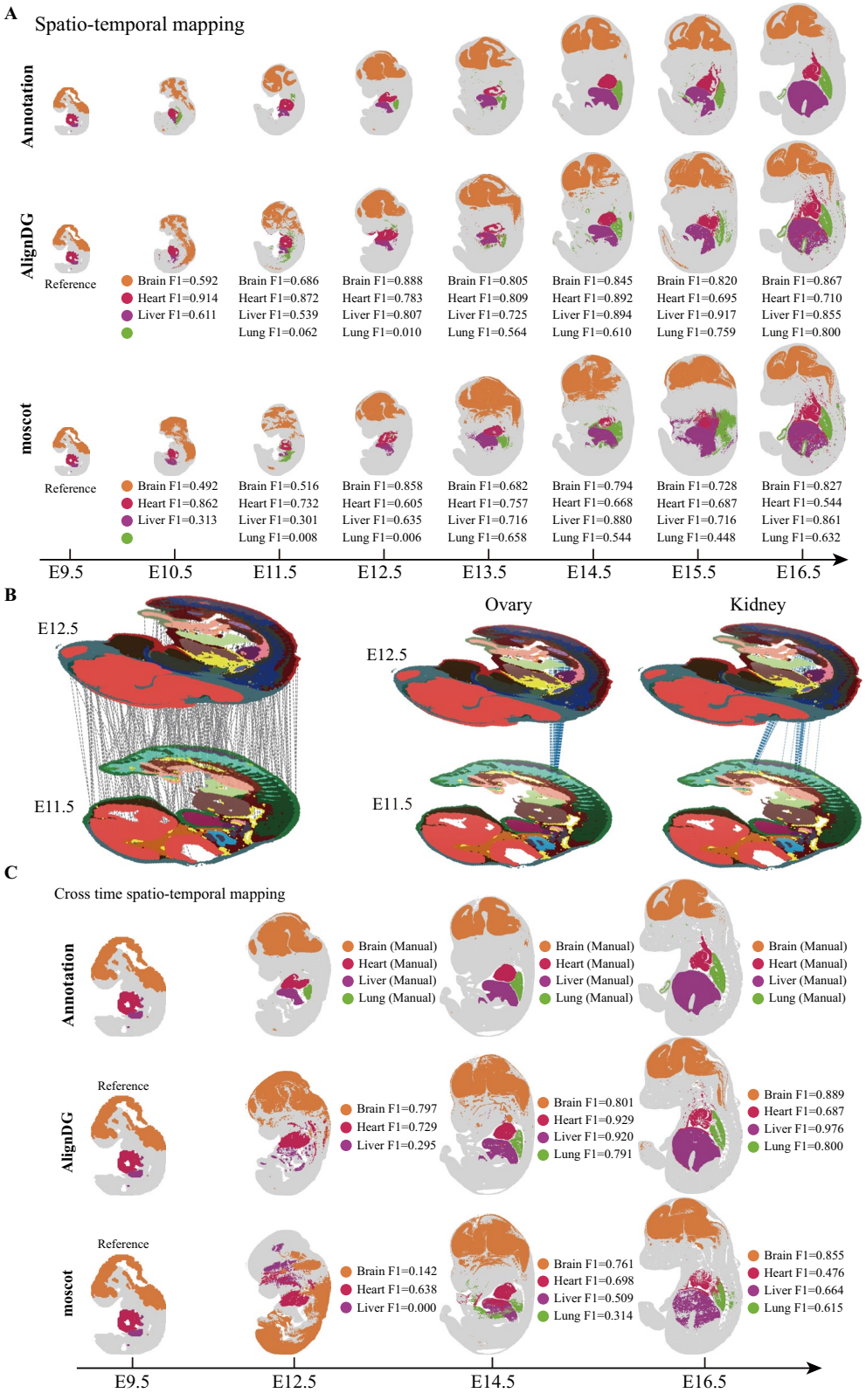

Fig. 5 AlignDG accurately aligns spatial-temporal slices associated with tissue development. **A** Visualization of major organs during the development of mouse embryo with continuous slice alignment (bottom), where F1-score measures similarity between the truth (top) and predicted organs at each time point. **B** Visualization of the alignment between E11.5 and E12.5 mouse embryo Stereo-seq datasets, colored by cell types (subsampled to 300 alignment pairs for clear visualization, left), and evolution of *Ovary* (middle) and *Kidney* (right). **C** Visualization of manual annotations (top) and predicted major organs associated with development of mouse embryo with alignment of non-consecutive slices by using AlignDG (middle) and Moscot (bottom)

F1-score=0.764 ± 0.134, Additional file 1: Fig. S23A). Notice that only AlignDG and Moscot can effectively address all slices from E9.5 to E16.5 as they utilize low-rank optimal transport to accelerate alignment, enabling their application to large-scale slices (Section: Methods).

To further exploit alignment of spatiotemporal slices, we analyze the mouse embryo dataset between E9.5 and E10.5, where AGM (aorta-gonad-mesonephros) cells at E9.5 is mapped to spatial domains in E10.5 (Additional file 1: Fig. S24A). It partially overlaps with annotated tissues, including Lung Primordium, Blood Vessel, Urogenital Ridge, Connective Tissue, and Spinal Cord (Additional file 1: Fig. S24B), and nearly 50% of bio-marker genes of AGM are overlapped with those of the aligned domains, indicating that the aligned tissues are highly related (Additional file 1: Fig. S24C top). Interestingly, these biomarker genes are highly expressed in different stages of tissues. For example, *Peg3* and *Gpc3* are well-known as progenitor cell marker, which is highly expressed in AGM at E9.5 and Lung Primorduim at E10.5 (Additional file 1: Fig. S24C bottom). *Hba-a1* (hemoglobin alpha, adult chain 1) and Blood Vessel cells at E10.5 (Additional file 1: Fig. S24C bottom). And, the spatial distribution patterns of overlapping biomarker genes between E9.5 and E10.5 are similar at the two subsequent time points (Additional file 1: Fig. S24D), suggesting that AlignDG effectively capatures genuine developmental transitions rather than producing arbitrary alignments. GO enrichment analysis show that biomarker genes are significantly enriched biological functions associated with development of tissues (Additional file 1: Fig. S24E), such as myeloid cell differentiation (adjusted p-value=4.5E-10, hyper-geometric test), regulation of epithelial cell proliferation (adjusted p-value=2.1E-3, hyper-geometric test), which are highly related to development of tissues [74, 75]. Alignment between E11.5 and E12.5 obtained by AlignDG (Fig. 5B left) demonstrates that *kidney* and *ovary* are initialized at E12.5, which are originated from *Urogenital Ridge* at E11.5 [76, 77]. In details, *ovary* emerges directly from one domain, and *kidney* is derived from two separate domains corresponding to the *mesonephros* and *metanephros* structures in early *kidney* [78, 79]. As shown in Fig. 5B (right panel), AlignDG precisely tracks the evolution of *kidney* and *ovary* across spatial-temporal slices. These results demonstrate that AlignDG captures biologically meaningful alignment across spatial-temporal slices, reflecting dynamics of tissue development.

Then, we validate performance of AlignDG for distant (non-continuous) slice alignment using a reduced number of slices. Specifically, we benchmark AlignDG with non-continuous slices between E9.5 and E12.5, E12.5 and E14.5, and E14.5 and E16.5, where approximately 50% of slices are removed from the original dataset. As shown in Fig. 5C, AlignDG precisely tracks development of major organs, demonstrating that AlignDG also applicable to non-continuous slice alignment (Additional file 1: Fig. 23B). More specifically, F1-score of AlignDG at E12.5 is 0.801 (brain), 0.929 (heart), 0.920 (liver), and 0.791 (lung), whereas that of Moscot is 0.761 (brain), 0.698 (heart), 0.509 (liver), and 0.314 (lung). These results confirm that AlignDG maintains comparable alignment performance even with a 50% reduction of slices, which is of great significance values because it enables substantial savings in both experimental and computational cost, benefiting both biological research and algorithm development.

Moreover, an additional dataset for axolotl brain regeneration [6] with 7 time points is also selected, which covers 2, 5, 10, 15, 20, 30, and 60 days post-injury (DPI) to dissect immediate wound responses and later regeneration processes (Additional file 1: Fig. S25A). Analogously, AlignDG tracks development of lineages with alignment, where *EGC* (epidermal germinative cell) transforms into *wntEGC* and *reaEGC* cells (Additional file 1: Fig. S25B). We speculate that these transformations are highly related to the degree of wound healing over time. Initially, when the wound is severe (at 2 DPI), *sfrpEGC* cells are directly transformed into *reaEGC* cells, or into *wntEGC* and *ribEGC* cells, which are then transformed into *reaEGC* cells. Later, as wound heals (from DPI 15 to DPI 20), *reaEGC* cells transform back into *wntEGC* cells or differentiate into other cells. Moreover, AlignDG also describes cell dynamics during axolotl brain regeneration. At the beginning of injury (from DPI 5 to DPI 10), *sfrpEGC* and *wntEGC* cells transform into *reaEGC* cells, and cell proliferation in the injured hemisphere activates, especially for *EGC*-type cells in the vicinity of the wound, and *reaEGC* cells move toward the wound. As the wound gradually healed, *reaEGC* cells transform back to *wntEGC* cells or differentiated into other types of neurons, which is consistent with assertions in Ref. [6, 80] (Additional file 1: Fig. S25C). To evaluate performance of AlignDG, an additional experiment for aligning distant slices is performed on the axolotl brain regeneration dataset, where AlignDG consistently achieves the best performance, thereby demonstrating its generality across species (Additional file 1: Fig. S26). These results further indicate that AlignDG is robust in aligning distant slices, requiring fewer slices than current baselines.

In summary, AlignDG provides a novel strategy for investigating the spatial-temporal dynamics of cellular differentiation, achieving comparable performance with about 50% slices, which may dramatically reduce burden of finance and labour for biologists.

AlignDG accurately identifies disease-related spatial domains with distant slice alignment

Previous experiments are devoted to the alignment of ST slices under identical conditions, and we extend our

evaluation to examine performance of AlignDG with slices under various experimental conditions for the identification of condition-specific spatial domains. Specifically, slices from normal and Alzheimer's disease (AD) hippocampus tissue of mouse profiled by Slide-seq V2 [5] annotated by the Allen Mouse Brain Atlas (Fig. 6A) are selected to validate whether distant alignment can identify disease-related spatial domains. Figure 6B visualizes embedding of slices (left panel, red for normal slice and blue for AD slice), and spatial domains identified by AlignDG, where these two slices are highly overlapping, indicating that AlignDG effectively removes batch effect. Notice that most regions are overlapped, while only few of them are unique (dashed circle in Fig. 6B left panel, Additional file 1: Fig. S27). Spatial domains identified by various algorithms are visualized in Fig. 6C, where AlignDG, STAligner, and SLAT identify the disease-related domain (Additional file 1: Fig. S27). Furthermore, most spatial domains identified by AlignDG reveal clear spatial patterns corresponding to anatomical structures of the hippocampus. Specifically, domain 4, 6 and 11 are conserved in both normal and disease slices, forming the 'cord-arrow-like' structure in the hippocampus region (Fig. 6C and Additional file 1: Fig. S28A), where domain 6 ('arrow-like') corresponds to the dentate gurys region, and domains 4 and 11 ('cord-like') correspond to the structure *CA3* and *CA1* of Ammon's horn, respectively. Interestingly, domain 13 is AD-specific, whereas others are shared by normal and AD slices at some extent (Additional file 1: Fig. S28B), potentially shedding light on revealing structure and functions of AD. Importantly, the high Aβ plaque density in the vicinity of domain 13 indicates that it is highly co-localized with the amyloid deposition, which is one of the key pathological features of AD (Fig. 6D).

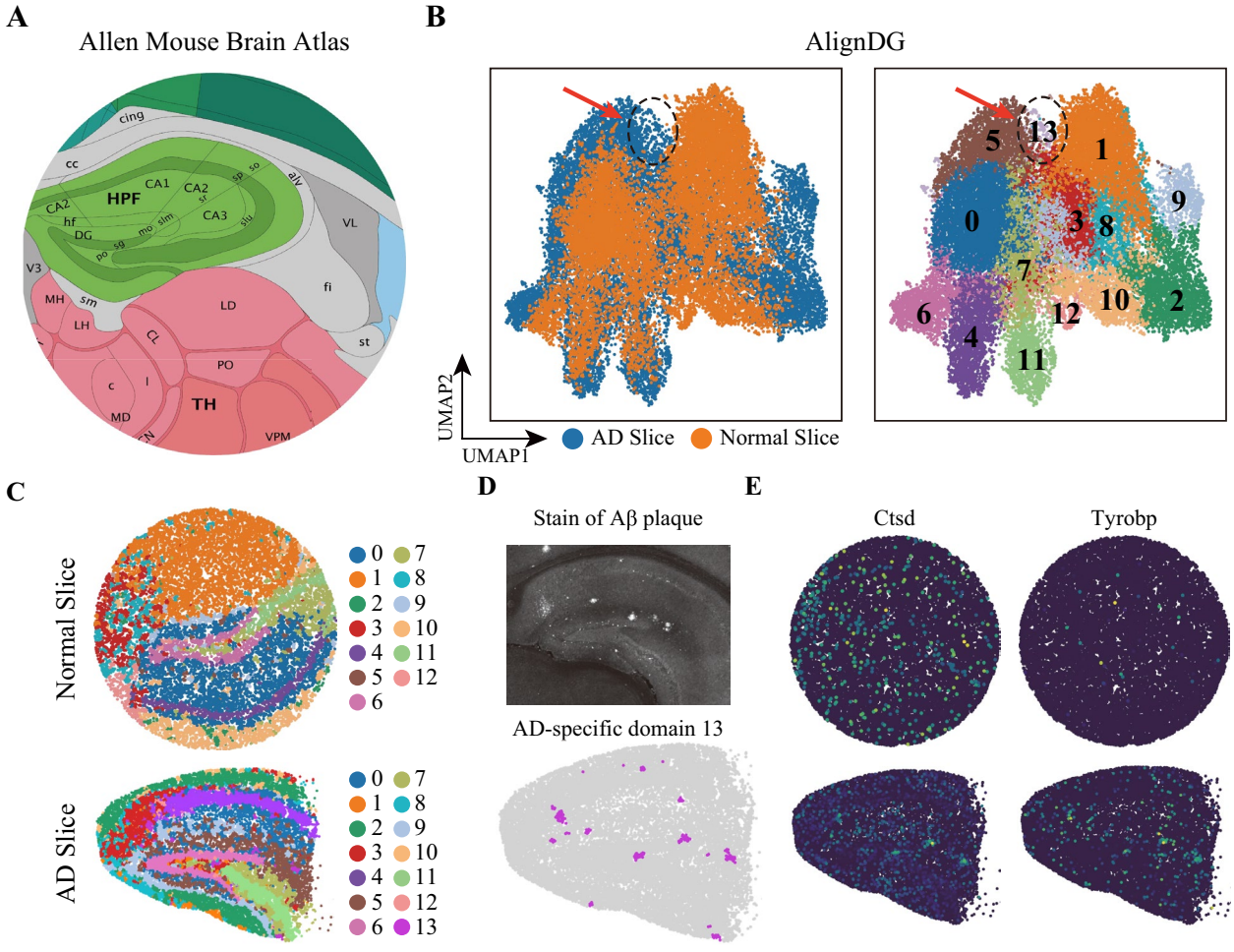

Fig. 6 AlignDG precisely identifies disease-related spatial domains with distant alignment between normal and disease slices. **A** Laminar organization of mouse hippocampus annotated by Allen Mouse Brain Atlas. **B** Visualization of spatial domains identified simultaneously by integrating and aligning the two ST slices profiled via AlignDG. **C** UMAP plots of AlignDG embeddings colored by spatial domains (left panel) and slices (right panel). **D** The antibody of Aβ. in the adjacent hippocampus slice (top) and the spatial distribution of spatial domain solely found in the AD slice (Bottom). **E** Spatial expression maps of marker gene *Tyrobp* for spatial domain 13 in the normal and AD slices

Since domain 1 and 13 are with highest percentage of normal and disease spots respectively (excluding the 'cord-arrow-like' structure), which are also proximity in feature space(Additional file 1: Fig. S28B). Differential expression analysis between domain 13 and 1 is performed to identify differentially expressed genes (DEGs, $|logFC| \geq 2$, p<5.0E-2, Wilcoxon rank-sum test for significance, Methods section, Fig. 6E, Additional file 1: Fig. S28C). Interestingly, *Tyrobp* is markedly up-regulated in Aβ-associated brain regions (p=7.1E-14), acting as the downstream adaptor and putative signaling partner for several receptors implicated in AD [81], enhancing the phagocytic activity of microglia and clearance of Aβ deposits (Additional file 1: Fig. S29A). Furthermore, it also participates in the initiation of inflammatory responses, and the latter may exacerbate neurodegenerative processes [82]. And, mutation of *Cst3* results in less efficient cleavage of the signal peptide and reduced secretion of Cystatin C secretion (p=1.8E-17), which is associated with increased risk of Alzheimer's disease [83]. Functional enrichment analysis shows that these DEGs are involved in *glial cell activation*, *macrophage activation*, *neuron apoptotic process*, and *alpha-beta T cell activation* (Additional file 1: Fig. S29B), which are highly associated with the progression of Alzheimer's disease [84]. And, evidence proves that *C1qb* and *C1qc* are strongly expressed by Aβ-associated microglia and mediate synapse loss in AD [85], where spatial expression distribution of *Tyrobp* is localized near the position of Aβ accumulation, illustrating the potential effect of Aβ accumulation on gene expression (Fig. 6E). These results demonstrate that AlignDG precisely captures the conserved and specific structures between normal and disease slices, proving the superiority of distant alignment. Furthermore, these findings further confirm that alignment of slices under heterogeneous conditions facilitates the identification of meta-structures of spots, i.e., spatial domains, demonstrating the potential application of AlignDG for cell annotation across ST datasets.

AlignDG facilitates 3D architecture of tissues with multiple slices

Recent studies demonstrate that tracking changes in the expression levels of biomarker genes within three-dimensional (3D) tissue architecture facilitates the identification of functional regions, characterization of cell state transitions and tissue-specific gene regulation, which are fundamental for elucidating mechanisms of complex diseases [86, 87]. Therefore, it is of great significance for reconstructing 3D architecture of tissues by integrating multiple consecutive slices. Here, we evaluate the performance of AlignDG in reconstructing 3D architecture of tissues. AlignDG is highly flexible and provides two different strategies for aligning multiple consecutive slices for 3D reconstruction, i.e., pairwise- and reference-based approach (Fig. 7A). The pairwise-based strategy (denoted as AlignDG-P) aligns each pair of consecutive slices and integrates all slices sequentially to perform 3D reconstruction (Fig. 7A top), and the reference-based approach (denoted as AlignDG-R) selects one slice as the reference, and aligns all other slices to the reference one (Fig. 7A bottom). The mathematical model is presented in section of Methods.

We then benchmark AlignDG-P and AlignDG-R against several state-of-the-art algorithms, such as PASTE [39], PASTE2 [33], SLAT [43], SPACEL [38], and Spateo [35], for the reconstruction of 3D architecture of tissues. By following Ref. [35], two measurements, including mean squared error and angle shift, are selected to measure performance of these algorithms on the human DLPFC (Fig. 7B) and mouse HPC dataset (Fig. 7C). Since no manually annotated spatial registration of these slices for 3D reconstruction is available, we employ the corrected spatial coordinates provided by PASTE [55] as the ground truth because of the improved spatial consistency across slices (Additional file 1: Fig. S30). And, manually corrected spatial information of mouse HPC dataset profiled by MERFISH is provided by Squidpy [49]. Figure 7B visualizes performance of various algorithms for the human DLPFC dataset, where each column corresponds to an algorithm, top panel is for the stacked aligned slices in 2D space (colored by slices), middle for 3D architecture obtained by various algorithms (colored by spatial domains), and bottom for spatial distribution of biomarker genes in 3D architecture (colored by expression level). From these these visualization results, it is easy to assert that 3D architecture constructed by AlignDG, PASTE2 and Spateo is much closer to the ground truth structures than others, demonstrating that these algorithms precisely reconstruct architecture of tissues. Furthermore, we quantify approximation of the reconstructed and ground truth 3D architecture in terms of mean squared error and angle shift (right panel of Fig. 7B), where the proposed algorithm is much better than baselines, indicating that AlignDG is also promising for 3D reconstruction by aligning multiple slices. In details, mean squared error is 73.227 of AlignDG-P (54.501 for AlignDG-R), whereas it is 145.554 for PASTE2, 9988.762 for SLAT, 1294.274 for STAligner, 152.675 for Moscot, 156.372 for SPACEL, 511.360 for Spateo, and 8666.034 for CAST, respectively. And, angle shift of AlignDG-P is 0.720 (0.693 for AlignDG-R), whereas it is 0.919 for PASTE2, 92.319 for SLAT, 5.564 for STAligner, 0.921 for Moscot, 1.823 for SPACEL, 1.591 for Spateo, 30.227 for CAST, respectively. Furthermore, AlignDG consistently outperforms other baselines on the MERFISH data (Fig. 7C), further demonstrating the platform invariance

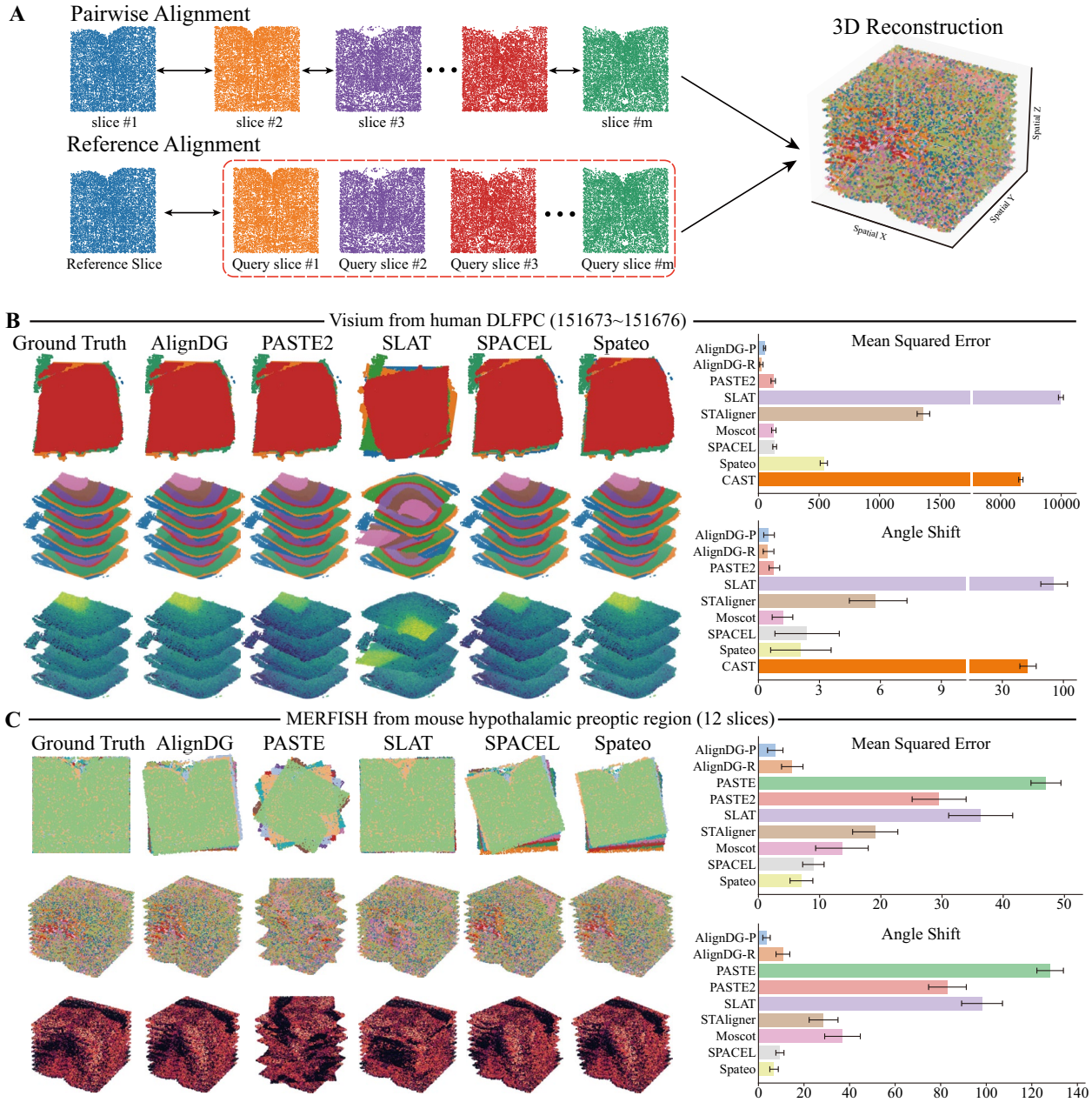

Fig. 7 Performance of AlignDG for 3D architecture of tissues with multiple slices. **A** pipelines for AlignDG for the reconstruction of 3D architecture, **B** Visium human DLPFC dataset, and **C** MERFISH mouse hypothalamic preoptic region dataset, where top panel is for 2D stack of all slices, mid panel for the reconstructed 3D architecture (colored by spatial domains), and bottom panel for spatial distribution of biomarker genes in the reconstructed 3D architecture (colored by expression level), respectively

and robust reconstruction capability of the proposed algorithm.

In all, AlignDG is also applicable for 3D architecture of tissues, demonstrating superiority of AlignDG for adjacent and distant alignment of ST slices.

Discussion

Slice alignment is a fundamental task in the analysis of ST data, and various algorithms are developed to address this biologically important challenge. However, current algorithms typically rely on manually annotated landmarks to guide slice alignments, or operate under the assumption of balanced slices with comparable sizes. Furthermore, available algorithms separate feature learning from alignment, resulting in undesirable performance. By integrating attributed network model with graph-based learning, AlignDG achieves reliable slice alignment for both adjacent and distant slices in an unsupervised and data-driven manner, which dramatically extends the applications of slice alignment. A summary of the

Table 1 Summary of current algorithms for alignment of ST slices, where ✓ denotes algorithms are applicable for the conditions

Method	Alignment (adjacent)	Batch correction	Spatial aware	Prior free	Large scale	Alignment (Unbalanced)	Alignment (Distant)
Seurat [24]	✓	✓		✓			
Harmony [26]	✓	✓		✓	✓		
SANTO [36]	✓		✓			✓	
STalign [34]	✓		✓			✓	
GraphST [66]	✓	✓	✓				
SLAT [43]	✓	✓	✓				✓
CAST [37]	✓	✓	✓	✓			
PASTE [39]	✓		✓	✓			
DeepST [11]	✓	✓	✓	✓			
PASTE2 [33]	✓		✓	✓		✓	
STAligner [41]	✓	✓	✓	✓			✓
SPACEL [38]	✓	✓	✓			✓	
Spateo [35]	✓		✓	✓	✓		
Moscot [45]	✓		✓		✓	✓	✓
AlignDG	✓	✓	✓	✓	✓	✓	✓

proposed algorithm and current baselines for alignment of ST slices is provided in Table 1. Overall, AlignDG provides a unified framework for aligning ST slices, and the source code and tutorials for AlignDG are also available at https://github.com/xkmaxidian/AlignDG.

The unique capability of AlignDG for distant slice alignment enables diverse biological applications, covering non-consecutive or non-continuous slices across different tissues, as well as slices from different conditions that are currently unmanageable by existing methods. Furthermore, alignment of distant slices enables the identification of spatially-resolved patterns, which not only bridges ST technologies with various resolutions and genomic coverage, but also detects key regulators and pathways of tissues. More importantly, AlignDG fulfills alignment of distant slices by saving about 50% of slices with a comparable performance, which is critical for biologists for launching and designing biological experiments. AlignDG is also efficient and applicable across various conditions that cannot be properly addressed by current state-of-the-art methods, where existing methods often decouple feature learning from alignment. And, AlignDG integrates feature learning and alignment of slices by dynamically updating features of spots, thereby significantly reducing computational complexity. Notably, only AlignDG and Moscot efficiently handle large-scale slices, performing alignment of slices with 100,000 spots within 20 minutes.

Furthermore, pan-cancer analysis [88–90] show that highly related diseases often share cancer-associated genes, and AlignDG provides an effective strategy to identify shared patterns by aligning distant slices across different diseases. Thus, we apply AlignDG to human breast and ovarian cancer slices generated by 10× Visium (Additional file 1: Fig. S31A), where both overlapping and non-overlapping spatial domains are observed, proving existence of specific and conserved spatial domains for breast and ovarian cancer (Additional file 1: Fig. S31B-C). Moreover, DEGs associated with conserved domains are largely overlapped between these two slices, demonstrating that breast and ovarian cancer are highly related [91–93] (Additional file 1: Fig. S31D, Fig. S32A). We also find that the biomarker genes associated with these shared domains (i.e., domains identified in both slices) are associated with the conserved spatial patterns of slices, which may provide novel insights into underlying biological mechanisms (Additional file 1: Fig. S31E-F, Supplementary Fig. S32B). For example, gene *HSP90AA1* encodes the heat shock protein HSP90α, which regulates tumor immunity and therapy response by modulating protein stability and stress-related signaling pathways. Inhibition of *HSP90AA1* activity reverses multi-drug resistance and reduces stem-like properties in immune-refractory tumors [94–96]. Consistently, we find that gene *HSP90AA1* significantly stratifies survival time of breast and ovarian cancer cohorts (breast cancer: p=2.6E-3, ovarian cancer: p=2.0E-2, Additional file 1: Fig. S31G). In addition, we also find that several biomarker genes can also predict survival time of patients, such as *CD24* and *JTB* (Additional file 1: Fig. S32C). These results demonstrate that alignment of slices across different diseases is promising for discovering potential biomarker genes. Notably, up-regulation of *HSP90AA1* (Additional file 1: Fig. 31 F) is associated with poor prognosis in breast cancer [97], which also links to improved prognosis of ovarian cancer [98], suggesting that functions of *HSP90AA1* may vary substantially across tumor microenvironments. Note that pan-cancer analysis require a great amount of samples to ensure reliability of patterns, and alignment of

distant slices across diseases also need further validation with more samples.

Despite its promising performance, AlignDG still has several limitations for further investigation. First, AlignDG does not account for local distortions that inevitably occur during the sequencing processes, which may require non-rigid spatial transformations. Addressing these distortion of ST slices is promising for extending the applicability of AlignDG. Second, AlignDG cannot be directly applied to extra-large-scale ST slices composed of multiple stitched regions. Developing more efficient strategies for stitching and aligning slices of large tissues is also great interesting. Third, although these image registration algorithms for medical images are not easily extended for slice alignment, how to fully make use of the typical advantages of these algorithms, such as contour recognition, could further improve the performance of AlignDG. Finally, AlignDG aligns ST slices without considering spatial multi-omics data, and how to improve alignment of slices by integrating omics data is also interesting. Actually, there are two possible directions to integrate spatial omics data. Specifically, AlignDG jointly learns features of spots by integrating spatial omics modalities beyond spatial transcriptomics, i.e., spatial proteomics or other assays, which further improves quality and interpretability of features of spots, thereby deepening biological insights of alignment of ST slices. And, AlignDG performs alignment of ST slices at the spot level, which can be dramatically improved by utilizing meta-structures of spots, such as spatial domains, which are identified based on spatial omics data. Moreover, the hierarchical knowledge of spatial omics data may also substantially reduce computational complexity of AlignDG, thereby extending it to extra-ordinary lagescale ST datasets.

Conclusions

We propose AlignDG, i.e., a novel network-based model designed for precise alignment and integration of ST slices without requiring prior information. In contrast to existing methods, AlignDG effectively handles challenging scenarios, such as non-consecutive, non-continuous, across different tissues and diseases conditions. In spatiotemporal ST datasets associated with development of tissues, AlignDG precisely tracks tissue development using only approximately 50% slices of datasets, providing biologists with a powerful tool to optimize experimental design and enhance the efficiency of data analysis.

Abbreviations

AD	Alzheimer's Disease
AOB	Accessory Olfactory Bulb
ARI	Adjusted Rand Index
CA1	Cornu Ammonis area 1
CA3	Cornu Ammonis area 3
cLISI	cell type Local Inverse Simpson's Index
DCIS	Ductal Carcinoma In Situ
DEG	Differentially Expressed Genes
DPI	Days Post Injury
EGC	Epidermal Germinative Cell
fMRI	functional Magnetic Resonance Imaging
GAT	Graph Auto-Encoder
GNN	Graph Neural Network
iLISI	integration Local Inverse Simpson's Index
KNN	K-Nearest Neighborhood
mRNA	messenger RNA
MNN	Mutual Nearest Neighbors
NMI	Normalized Mutual Information
OD	Oligodendrocyte
OFB	Olfactory Bulb
PAA	Pairwise Alignment Accuracy
scRNA-seq	single-cell RNA sequencing
SMR	Spot-to-spot Matching Ratio
ST	Spatial Transcriptomics
UMAP	Uniform Manifold Approximation and Projection
WM	White Matter

Supplementary Information

The online version contains supplementary material available at https://doi.org/10.1186/s13073-026-01634-w.

Additional file 1. Supplementary Materials of AlignDG, including the detailed derivations of the proposed AlignDG algorithm, the specific parameter settings of AlignDG for all datasets involved in this study, and all supplementary figures.

Acknowledgements

We thank the members of the Ma Lab for helpful discussion, and we particularly thank Prof. Qingchen Zhang for his support. We appreciate the researchers who provide us with source code for a comparison, and reviewers for their time and suggestions.

Authors' contributions

X.M. conceived and designed the study. X.M. and Y.W. performed the research. X.M., Z.L. and Y.W. collected and constructed the benchmark datasets and models. Y.W., Q.Z. and Z.L. completed the downstream analysis. All authors read and approved the final manuscript.

Funding

This work was supported by the Noncommunicable Chronic Diseases-National Science and Technology Major Project (2024ZD0531100, 2024ZD0531103), Joint Funds of the National Natural Science Foundation of China (U22A20345), National Natural Science Foundation of China (62272361), Natural Science Basic Research Program of Shaanxi (2025JC-QYCX-057), Xidian University Specially Funded Project for Interdisciplinary Exploration (TZJHF202507), and Fundamental Research Funds for the Central Universities and the Innovation Fund of Xidian University (YJSJ25012).

Data availability

The code for AlignDG algorithm is implemented in Python and detailed tutorials are freely available at Github as well as Zendo [99, 100]. The source code of AlignDG is released under the MIT License. All datasets analyzed in this paper are published datasets available for download. The simulated datasets are generated using Splatter and are accessible at https://github.com/xkmaxidian/AlignDG. The human DLPFC slices are accessible within the SpatialLIBD at http://spatial.libd.org/spatialLIBD. The mouse hypothalamic preoptic slices sequenced by MERFISH are accessible at https://zhuang.harvard.edu/merfish. The whole mouse embryo slices sequenced by Stereo-seq are accessible at https://db.cngb.org/stomics/mosta/download. And the E8.75 mouse embryo sequenced by seqFISH is accessible at https://marionilab.cruk.cam.ac.uk/SpatialMouseAtlas. The mouse olfactory bulb slices sequenced by Slide-seq V2 and Stereo-seq are available at https://singlecell.broadinstitute.org/single_cell/study/SCP815 and https://github.com/JinmiaoChenLab/SEDR_analyses. The axolotl brain spatiotemporal slices sequenced by Stereo-seq are available at https://db.cngb.org/stomics/artista. The normal and Alzheimer's disease mouse hippocampus slices sequenced by Slide-seq V2 can be accessed at https://si

nglecell.broadinstitute.org/single_cell/study/SCP815 and https://singlecell.broadinstitute.org/single_cell/study/SCP1663, respectively. The breast cancer slices co-assayed by 10X Visium and Xenium, and the Ovarian cancer slice are collected from the 10X Genomics website at https://www.10xgenomics.com/resources/datasets.

Declarations

Ethics approval and consent to participate

No ethical approval was required for this study. All utilized public datasets were generated by other organizations that obtained ethical approval.

Consent for publication

Not applicable.

Competing interests

The authors declare no competing interests.

Received: 23 May 2025 / Accepted: 23 March 2026
Published online: 02 April 2026

References

1. Marx V. Method of the year: spatially resolved transcriptomics. Nat Methods. 2021;18(1):9–14.
2. Bressan D, Battistoni G, Hannon GJ. The dawn of spatial omics. Science. 2023;381(6657):eabq4964.
3. Ståhl PL, Salmén F, Vickovic S, Lundmark A, Navarro JF, Magnusson J, et al. Visualization and analysis of gene expression in tissue sections by spatial transcriptomics. Science. 2016;353:78–82.
4. Rodriques SG, Stickels RR, Goeva A, Martin CA, Murray E, Vanderburg CR, et al. Slide-seq: a scalable technology for measuring genome-wide expression at high spatial resolution. Science. 2019;363:1463–7.
5. Stickels RR, Murray E, Kumar P, Li J, Marshall JL, Di Bella DJ, et al. Highly sensitive spatial transcriptomics at near-cellular resolution with Slide-seqV2. Nat Biotechnol. 2021;39:313–9.
6. Wei X, Fu S, Li H, Liu Y, Wang S, Feng W, et al. Single-cell stereo-seq reveals induced progenitor cells involved in axolotl brain regeneration. Science. 2022;377:eabp9444.
7. Hu J, Li X, Coleman K, Schroeder A, Ma N, Irwin DJ, et al. SpaGCN: Integrating gene expression, spatial location and histology to identify spatial domains and spatially variable genes by graph convolutional network. Nat Methods. 2021;18:1342–51.
8. Zhao E, Stone MR, Ren X, Guenthoer J, Smythe KS, Pulliam T, et al. Spatial transcriptomics at subspot resolution with bayesSpace. Nat Biotechnol. 2021;39:1375–84.
9. Shang L, Zhou X. Spatially aware dimension reduction for spatial transcriptomics. Nat Commun. 2022;13:7203.
10. Li J, Chen S, Pan X, Yuan Y, Shen HB. Cell clustering for spatial transcriptomics data with graph neural networks. Nat Comput Sci. 2022;2:399–408.
11. Xu C, Jin X, Wei S, Wang P, Luo M, Xu Z, et al. DeepST: identifying spatial domains in spatial transcriptomics by deep learning. Nucleic Acids Res. 2022;50:e131–e131.
12. Dong K, Zhang S. Deciphering spatial domains from spatially resolved transcriptomics with an adaptive graph attention auto-encoder. Nat Commun. 2022;13:1–12.
13. Zuo C, Zhang Y, Cao C, Feng J, Jiao M, Chen L. Elucidating tumor heterogeneity from spatially resolved transcriptomics data by multi-view graph collaborative learning. Nat Commun. 2022;13(1):5962.
14. Liu W, Liao X, Yang Y, Lin H, Yeong J, Zhou X, et al. Joint dimension reduction and clustering analysis of single-cell RNA-seq and spatial transcriptomics data. Nucleic Acids Res. 2022;50(12):e72–e72.
15. Wang Y, Liu Z, Ma X. MNMST: topology of cell networks leverages identification of spatial domains from spatial transcriptomics data. Genome Biol. 2024;25(1):133.
16. Cable DM, Murray E, Zou LS, Goeva A, Macosko EZ, Chen F, et al. Robust decomposition of cell type mixtures in spatial transcriptomics. Nat Biotechnol. 2022;40(4):517–26.
17. Li B, Zhang W, Guo C, Xu H, Li L, Fang M, et al. Benchmarking spatial and single-cell transcriptomics integration methods for transcript distribution prediction and cell type deconvolution. Nat Methods. 2022;19(6):662–70.
18. Pham D, Tan X, Balderson B, Xu J, Grice LF, Yoon S, et al. Robust mapping of spatiotemporal trajectories and cell-cell interactions in healthy and diseased tissues. Nat Commun. 2023;14(1):7739.
19. Moses L, Pachter L. Museum of spatial transcriptomics. Nat Methods. 2022;19(5):534–46.
20. Yuan Z, Pan W, Zhao X, Zhao F, Xu Z, Li X, et al. SODB facilitates comprehensive exploration of spatial omics data. Nat Methods. 2023;20(3):387–99.
21. You Y, Fu Y, Li L, Zhang Z, Jia S, Lu S, et al. Systematic comparison of sequencing-based spatial transcriptomic methods. Nat Methods. 2024. https://doi.org/10.1038/s41592-024-02325-3.
22. Xiong YX, Zhang XF. Scdot: enhancing single-cell rna-seq data annotation and uncovering novel cell types through multi-reference integration. Brief Bioinform. 2024;25(2):bbae072.
23. Gao Z, Cao K, Wan L. Graspot: a graph attention network for spatial transcriptomics data integration with optimal transport. Bioinformatics. 2024;40(Supplement_2):ii137–45.
24. Stuart T, Butler A, Hoffman P, Hafemeister C, Papalexi E, Mauck WM, et al. Comprehensive integration of single-cell data. Cell. 2019;177(7):1888–902.
25. Thompson B. Canonical correlation analysis: Uses and interpretation, vol. 47. Sage; 1984.
26. Korsunsky I, Millard N, Fan J, Slowikowski K, Zhang F, Wei K, et al. Fast, sensitive and accurate integration of single-cell data with Harmony. Nat Methods. 2019;16(12):1289–96.
27. Lopez R, Regier J, Cole MB, Jordan MI, Yosef N. Deep generative modeling for single-cell transcriptomics. Nat Methods. 2018;15(12):1053–8.
28. Woo J, Stone M, Prince JL. Multimodal registration via mutual information incorporating geometric and spatial context. IEEE Trans Image Process. 2015;24(2):757–69.
29. Loeckx D, Slagmolen P, Maes F, Vandermeulen D, Suetens P. Nonrigid image registration using conditional mutual information. IEEE Trans Med Imaging. 2010;29(1):19–29.
30. Sotiras A, Davatzikos C, Paragios N. Deformable medical image registration: a survey. IEEE Trans Med Imaging. 2013;32(1):1153–90.
31. Klein A, Andersson J, Ardekani B, et al. Evaluation of 14 nonlinear deformation algorithms applied to human brain MRI registration. Neuroimage. 2009;46:786–802.
32. Jones A, Townes FW, Li D, Engelhardt BE. Alignment of spatial genomics data using deep Gaussian processes. Nat Methods. 2023;20:1379–87.
33. Liu X, Zeira R, Raphael BJ. Partial alignment of multislice spatially resolved transcriptomics data. Genome Res. 2023;33(7):1124–32.
34. Clifton K, Anant M, Aihara G, Atta L, Aimiuwu OK, Kebschull JM, et al. STalign: Alignment of spatial transcriptomics data using diffeomorphic metric mapping. Nat Commun. 2023;14(1):8123.
35. Qiu X, Zhu DY, Lu Y, Yao J, Jing Z, Min KH, et al. Spatiotemporal modeling of molecular holograms. Cell. 2024;187(26):7351–73.
36. Li H, Lin Y, He W, Han W, Xu X, Xu C, et al. SANTO: a coarse-to-fine alignment and stitching method for spatial omics. Nat Commun. 2024;15(1):6048.
37. Tang Z, Luo S, Zeng H, Huang J, Sui X, Wu M, et al. Search and match across spatial omics samples at single-cell resolution. Nat Methods. 2024. https://doi.org/10.1038/s41592-024-02410-7.
38. Xu H, Wang S, Fang M, Luo S, Chen C, Wan S, et al. SPACEL: deep learning-based characterization of spatial transcriptome architectures. Nat Commun. 2023;14(1):7603.
39. Zeira R, Land M, Strzalkowski A, Raphael BJ. Alignment and integration of spatial transcriptomics data. Nat Methods. 2022;19(5):567–75.
40. Halmos P, Liu X, Gold J, Chen F, Ding L, Raphael BJ. DeST-OT: Alignment of Spatiotemporal Transcriptomics Data. In: International Conference on Research in Computational Molecular Biology. Springer; 2024. pp. 434–437.
41. Zhou X, Dong K, Zhang S. Integrating spatial transcriptomics data across different conditions, technologies and developmental stages. Nat Comput Sci. 2023;3(10):894–906.
42. Haghverdi L, Lun AT, Morgan MD, Marioni JC. Batch effects in single-cell RNA-sequencing data are corrected by matching mutual nearest neighbors. Nat Biotechnol. 2018;36(5):421–7.
43. Xia CR, Cao ZJ, Tu XM, Gao G. Spatial-linked alignment tool (SLAT) for aligning heterogenous slices. Nat Commun. 2023;14(1):7236.
44. Gao J, Huang X, Li J. Unsupervised graph alignment with wasserstein distance discriminator. In: Proceedings of the 27th ACM SIGKDD Conference

on Knowledge Discovery & Data Mining. 2021. pp. 426–435. Virtual Event, Singapore
45. Klein D, Palla G, Lange M, Klein M, Piran Z, Gander M, et al. Mapping cells through time and space with moscot. Nature. 2025. https://doi.org/10.1038/s41586-024-08453-2.
46. Wang C, Jiang P, Zhang X, Wang P, Qin T, Guan X. GTCAlign: Global Topology Consistency-based Graph Alignment. IEEE Trans Knowl Data Eng. 2024, 36(5): 2009-2025 .
47. Wolf FA, Angerer P, Theis FJ. SCANPY: large-scale single-cell gene expression data analysis. Genome Biol. 2018;19:1–5.
48. Satija R, Farrell JA, Gennert D, Schier AF, Regev A. Spatial reconstruction of single-cell gene expression data. Nat Biotechnol. 2015;33(5):495–502.
49. Palla G, Spitzer H, Klein M, Fischer D, Schaar AC, Kuemmerle LB, et al. Squidpy: a scalable framework for spatial omics analysis. Nat Methods. 2022;19:171–8.
50. Salehi A, Davulcu H. Graph attention auto-encoders. 2019. arXiv preprint arXiv:1905.10715.
51. Titouan V, Courty N, Tavenard R, Flamary R. Optimal transport for structured data with application on graphs. In: International Conference on Machine Learning. PMLR; 2019. pp. 6275–6284.
52. Scetbon M, Klein M, Palla G, Cuturi M. Unbalanced Low-rank Optimal Transport Solvers. Adv. Neural Inf. Process Syst. 2024;36:52312–25.
53. Wahba G. A least squares estimate of satellite attitude. SIAM Rev. 1965;7(3):409.
54. Kabsch W. A solution for the best rotation to relate two sets of vectors. Acta Crystallogr A. 1976;32(5):922–3.
55. Hu Y, Xie M, Li Y, Rao M, Shen W, Luo C, et al. Benchmarking clustering, alignment, and integration methods for spatial transcriptomics. Genome Biol. 2024;25(1):212.
56. Hubert L, Arabie P. Comparing partitions. J Classif. 1985;2:193–218.
57. Traag VA, Waltman L, Van Eck NJ. From louvain to leiden: guaranteeing well-connected communities. Sci Rep. 2019;9(1):1–12.
58. Levine JH, Simonds EF, Bendall SC, Davis KL, El-ad DA, Tadmor MD, et al. Data-driven phenotypic dissection of AML reveals progenitor-like cells that correlate with prognosis. Cell. 2015;162(1):184–97.
59. Becht E, McInnes L, Healy J, Dutertre CA, Kwok IW, Ng LG, et al. Dimensionality reduction for visualizing single-cell data using UMAP. Nat Biotechnol. 2019;37:38–44.
60. Wu T, Hu E, Xu S, Chen M, Guo P, Dai Z, et al. clusterProfiler 4.0: A universal enrichment tool for interpreting omics data. Innovation. 2021;2:100141.
61. Maynard KR, Collado-Torres L, Weber LM, Uytingco C, Barry BK, Williams SR, et al. Transcriptome-scale spatial gene expression in the human dorsolateral prefrontal cortex. Nat Neurosci. 2021;24:425–36.
62. Moffitt JR, Hao J, Wang G, Chen KH, Babcock HP, Zhuang X. High-throughput single-cell gene-expression profiling with multiplexed error-robust fluorescence in situ hybridization. Proc Natl Acad Sci U S A. 2016;113:11046–51.
63. Eng CHL, Lawson M, Zhu Q, Dries R, Koulena N, Takei Y, et al. Transcriptome-scale super-resolved imaging in tissues by RNA seqFISH+. Nature. 2019;568(7751):235–9.
64. Janesick A, Shelansky R, Gottscho AD, Wagner F, Williams SR, Rouault M, et al. High resolution mapping of the tumor microenvironment using integrated single-cell, spatial and in situ analysis. Nat Commun. 2023;14(1):8353.
65. Zappia L, Phipson B, Oshlack A. Splatter: simulation of single-cell RNA sequencing data. Genome Biol. 2017;18(1):174.
66. Long Y, Ang KS, Li M, Chong KLK, Sethi R, Zhong C, et al. Spatially informed clustering, integration, and deconvolution of spatial transcriptomics with GraphST. Nat Commun. 2023;14(1):1155.
67. Luecken MD, Büttner M, Chaichoompu K, Danese A, Interlandi M, Müller MF, et al. Benchmarking atlas-level data integration in single-cell genomics. Nat Methods. 2022;19(1):41–50.
68. Moffitt JR, Bambah-Mukku D, Eichhorn SW, Vaughn E, Shekhar K, Perez JD, et al. Molecular, spatial, and functional single-cell profiling of the hypothalamic preoptic region. Science. 2018;362(6416):eaau5324.
69. Chen A, Liao S, Cheng M, Ma K, Wu L, Lai Y, et al. Spatiotemporal transcriptomic atlas of mouse organogenesis using DNA nanoball-patterned arrays. Cell. 2022;185(10):1777–92.
70. Zhang D, Schreoeder A, Yan H, et al. Inferring super-resolution tissue architecture by integrating spatial transcriptomics with histology. Nat Biotechnol. 2024;42:1372–7.
71. Xu H, Fu H, Long Y, Ang KS, Sethi R, Chong K, et al. Unsupervised spatially embedded deep representation of spatial transcriptomics. Genome Med. 2024;16(1):12.
72. Sunkin SM, Ng L, Lau C, Dolbeare T, Gilbert TL, Thompson CL, et al. Allen brain atlas: an integrated spatio-temporal portal for exploring the central nervous system. Nucleic Acids Res. 2012;41:D996-1008.
73. Lohoff T, Ghazanfar S, Missarova A, Koulena N, Pierson N, Griffiths J, et al. Integration of spatial and single-cell transcriptomic data elucidates mouse organogenesis. Nat Biotechnol. 2022;40(1):74–85.
74. Li LL, Keverne E, Aparicio S, Ishino F, Barton S, Surani M. Regulation of maternal behavior and offspring growth by paternally expressed Peg3. Science. 1999;284(5412):330–4.
75. Butcher JT, Johnson T, Beers J, Columbus L, Isakson BE. Hemoglobin α in the blood vessel wall. Free Radic Biol Med. 2014;73:136–42.
76. Harding SD, Armit C, Armstrong J, Brennan J, Cheng Y, Haggarty B, et al. The GUDMAP database-an online resource for genitourinary research. Development. 2011;138(13):2845–53.
77. Cao J, Spielmann M, Qiu X, Huang X, Ibrahim DM, Hill AJ, et al. The single-cell transcriptional landscape of mammalian organogenesis. Nature. 2019;566(7745):496–502.
78. Bouchard M. Transcriptional control of kidney development. Differentiation. 2004;72(7):295–306.
79. Reidy KJ, Rosenblum ND. Cell and molecular biology of kidney development. In: Semin Nephrol, vol. 29. Elsevier; 2009. pp. 321–337.
80. Chen L, Li J, Ou Y, Kang M, Deng J, Wang Y, et al. The axolotl kidney: a novel model to study kidney regeneration. Kidney Int. 2023;104(3):599–604.
81. Haure-Mirande JV, Audrain M, Ehrlich ME, Gandy S. Microglial TYROBP/DAP12 in Alzheimer's disease: transduction of physiological and pathological signals across TREM2. Mol Neurodegener. 2022;17(1):55.
82. Zhao Y, Wu X, Li X, Jiang LL, Gui X, Liu Y, et al. TREM2 is a receptor for β-amyloid that mediates microglial function. Neuron. 2018;97(5):1023–31.
83. Cable DM, Murray E, Shanmugam V, Zhang S, Zou LS, Diao M, et al. Cell type-specific inference of differential expression in spatial transcriptomics. Nat Methods. 2022;19(9):1076–87.
84. Mi W, Pawlik M, Sastre M, Jung SS, Radvinsky DS, Klein AM, et al. Cystatin C inhibits amyloid-β deposition in Alzheimer's disease mouse models. Nat Genet. 2007;39(12):1440–2.
85. Hong S, Beja-Glasser VF, Nfonoyim BM, Frouin A, Li S, Ramakrishnan S, et al. Complement and microglia mediate early synapse loss in Alzheimer mouse models. Science. 2016;352(6286):712–6.
86. Wang M, Hu Q, Lv T, Wang Y, Lan Q, Xiang R, et al. High-resolution 3D spatiotemporal transcriptomic maps of developing Drosophila embryos and larvae. Dev Cell. 2022;57(10):1271–83.
87. Xiao Z, Cui L, Yuan Y, He N, Xie X, Lin S, et al. 3D reconstruction of a gastrulating human embryo. Cell. 2024;187(11):2855–74.
88. Martínez-Jiménez F, Movasati A, Brunner SR, et al. Pan-cancer whole-genome comparison of primary and metastatic solid tumours. Nature. 2023;618:333–341.
89. Liu J, Lichtenberg T, Hoadley KA, et al. An integrated TCGA pan-cancer clinical data resource to drive high-quality survival outcome analytics. Cell. 2018;173(2):400–16.
90. Berger AC, Korkut A, Kanchi RS, et al. A comprehensive pan-cancer molecular study of gynecologic and breast cancers. Cancer Cell. 2018;33(4):690–705.
91. Daly MB, Pal T, Berry MP, Buys SS, Dickson P, Domchek SM, et al. Genetic/familial high-risk assessment: breast, ovarian, and pancreatic, version 2.2021, NCCN clinical practice guidelines in oncology. J Natl Compr Cancer Netw. 2021;19(1):77–102.
92. Petrucelli N, Daly MB, Pal T. BRCA1-and BRCA2-associated hereditary breast and ovarian cancer. GeneReviews. 2022.
93. Gaba F, Goyal S, Marks D, Chandrasekaran D, Evans O, Robbani S, et al. Surgical decision making in premenopausal BRCA carriers considering risk-reducing early salpingectomy or salpingo-oophorectomy: a qualitative study. J Med Genet. 2022;59(2):122–32.
94. Eustace BK, Sakurai T, Stewart JK, Yimlamai D, Unger C, Zehetmeier C, et al. Functional proteomic screens reveal an essential extracellular role for hsp90α in cancer cell invasiveness. Nat Cell Biol. 2004;6(6):507–14.
95. Whitesell L, Lindquist SL. HSP90 and the chaperoning of cancer. Nat Rev Cancer. 2005;5(10):761–72.
96. Song KH, Oh SJ, Kim S, Cho H, Lee HJ, Song JS, et al. HSP90A inhibition promotes anti-tumor immunity by reversing multi-modal resistance and stem-like property of immune-refractory tumors. Nat Commun. 2020;11(1):562.
97. Cheng Q, Chang JT, Geradts J, Neckers LM, Haystead T, Spector NL, et al. Amplification and high-level expression of heat shock protein 90 marks aggressive phenotypes of human epidermal growth factor receptor 2 negative breast cancer. Breast Cancer Res. 2012;14:1–15.

98. Liu H, Xiao F, Serebriiskii IG, O'Brien SW, Maglaty MA, Astsaturov I, et al. Network analysis identifies an HSP90-central hub susceptible in ovarian cancer. Clin Cancer Res. 2013;19(18):5053–67.
99. Wang Y, Liu Z, Wang Q, Ma X. Alignment of distant spatially resolved transcriptomics slices across diseases, platforms and conditions with large gaps. GitHub. 2026. https://github.com/xkmaxidian/AlignDG.
100. Wang Y, Liu Z, Wang Q, Ma X. Alignment of distant spatially resolved transcriptomics slices across diseases, platforms and conditions with large gaps. Zenodo. 2026. https://zenodo.org/records/14724786.

Publisher's Note